

Electronic effects on the radiation damage in high-entropy alloys

Okan K. Orhan, Mohamed Hendy, Mauricio Ponga ^{*}

Department of Mechanical Engineering, University of British Columbia, 2054 - 6250 Applied Science Lane, Vancouver, BC, V6T 1Z4, Canada



ARTICLE INFO

Keywords:

High-entropy alloys
Radiation-damage resistance
Density-functional theory
Molecular dynamics

ABSTRACT

High-entropy alloys (HEAs) are exceptional candidates for radiation-resistant materials due to their complex local chemical environment and slow defect migration. Despite commonly overlooked, electronic effects on defects evolution in radiation environments also play a crucial role by dissipating excess energy through electron-phonon coupling and electronic heat conduction during cascade events. We present a systematic study on electronic properties in random-solid solutions (RSS) in four and five principal elements HEAs and their effect on defect formation, clustering, and recombination. Electronic properties, including electron-phonon coupling factor (G_{e-ph}), the electronic specific heat (C_e), and the electronic thermal conductivity (κ_e), are computed within first-principles calculations. Using the two-temperature molecular dynamics simulations, we show that the electron-phonon coupling factor and electronic specific heat play a critical role in Frenkel pairs formation. Specifically, the electron-phonon coupling factor quickly dissipates the kinetic energy during primary knock-on atom events via plasmon excitations and is subsequently dissipated via the free-electrons conduction. We show that these effects are more critical than the elastic distortion effects produced by the atomic mismatch. Of tremendous interest, we show that including lighter elements helps to increase G_{e-ph} suggesting the possibility to improve radiation resistance in HEA through optimal composition.

1. Introduction

High-entropy alloys (HEA) are *mostly* single-phased multi-principal-elements (MPE) alloys, often produced by *nearly* equimolar mixing of four, or more elements [1–3]. HEAs have been shown to exhibit exceptional thermal stability [4], hardness and strength [5–10], wear resistance [11,12], and oxidation resistance [11,13]. In particular, the equimolar chromium-cobalt-iron-nickel HEA (CrFeCoNi) has attracted considerable interest as it can serve as a base template to exploring non-equimolar compositions, or adding other elements such as manganese (Mn), copper (Cu), aluminum (Al), titanium (Ti), niobium (Nb), molybdenum (Mo) and many more to achieve exceptional materials properties [14–21].

In high-radiation environments, highly energetic particle beams excite primary knock-on atoms (PKAs) out when they travel through solids, which in turn create self-interstitial atoms (SIA) and vacancies, called Frenkel pairs (FPs). Formation and clustering of FPs locally distort lattices, resulting in dislocation loops and void growth. As these FPs recombine and migrate through the lattice, they generate significant microstructural changes over time, critically affecting the mechanical properties of materials subjected to radiation environments. Clustering

of defected atoms commonly reduces the structural integrity of materials by causing swelling, creep, and irradiation-induced stress corrosion cracking [22].

In the case of HEA, the complex local chemical environment and atomic-size mismatch create well-known elastic lattice distortions and core effects such as sluggish diffusion kinetics [3]. These effects help to reduce defect formation, slow down defect diffusion and accumulation, and promote vacancy-interstitial recombination, leading to lower radiation damage compared to pure metals and traditional alloys [23,24]. For instance, CrMnFeCoNi preserves its majority face-centered cubic phase even over 40 DPA irradiation throughout the temperature range of ~ 298 – 773 K [25]. Thus, HEAs are promising candidates for structural materials exposed to high-radiation environments [18,26] such as in nuclear reactors [18,27] and other environments such as space applications [26].

Due to the many challenges that appear during the testing of materials under radiation environments, experimental studies are difficult to perform and time-consuming. At the same time, since the formation, migration, clustering, as well as recombination of defects occur within a few femtoseconds (fs) to nanoseconds (ns) of the primary cascade event, it is pretty challenging to *in-situ* unravel mechanisms behind the defect

* Corresponding author.

E-mail address: mponga@mech.ubc.ca (M. Ponga).

evolution. Thus, the community heavily relies on numerical simulations to understand and predict radiation damage under radiation, especially for novel materials. In that sense, atomistic simulations based on either molecular dynamics (MD) or *ab-initio* molecular dynamics provide a framework to study materials under radiation environments systematically [18,28]. Being an atomistic technique, MD fully resolves the time and atomic environment and naturally describes the interactions between PKA and lattice, generating defects as the PKA loses its energy. These insights can then be incorporated in Monte-Carlo codes to predict damage in macroscopic specimens such as those used in engineering applications [29]. However, a drawback of classical MD is that it neglects electronic effects in materials.

In metallic materials such as HEA, the excess energy due to high-radiation exposure is deposited into phonons and electrons, resulting in defect formation and microstructural changes. Remarkably, the primary heat carriers in metallic materials are free electrons, which result in thermal conductivities that are much higher than the lattice contribution [30]. However, in MPE alloys, these contributions have to be carefully analyzed since they might change depending on the composition and defect population [31,32]. Therefore, incorporating electronic effects in radiation damage is paramount for metallic materials to accurately understand and predict the damage.

Due to the potential applications of MPE alloys as radiation-resistant materials, several studies have recently investigated their performance using a combination of experiments and numerical simulations, providing a fundamental understanding of the damage mechanisms during radiation in MPE alloys [28,33–36]. Remarkably, while the numerical simulations carried out in these studies include phonon effects in MPE alloys, electronic effects have been almost completely ignored in these works, making these results applicable -but also essentially limited- to small PKA energies. In particular, electronic effects become more predominant at moderate to high PKA energies since they trigger extremely high *electronic* temperatures, as locally observed on irradiated surfaces [37]. However, MD lacks quantum-mechanical effects required to capture electronic and electron-phonon (*e – ph*) coupling effects. Even though MD is a classical technique, is it possible to partially incorporate electronic effects within semi-empirical approaches such as the *so-called* two-temperature model [38–48]. However, these models require several temperature-dependent material parameters that are challenging to compute and, in many cases, remain unavailable. This lack of parameters is more accentuated in novel materials where properties are unavailable to the scientific community.

First-principles simulations provide valuable insights into the electronic properties of materials, especially in novel compositions. Typically, such simulations are heavily constrained by system size and spatial complexity [49,50]. In particular, it is challenging to accurately represent statistical representation of configurational disorderliness as in HEA cases as the number of simulation cells increases quickly with number of atoms and species. Indeed, if we let N_e be the number of atomic species (or elements), N_s be the number of sites in a multi-principal element metallic alloy, and N_i be the number of atoms of the i -th element, and using the combination notation, the number of

possible representations (N_{cells}) becomes $N_{\text{cells}} = \prod_{i=1}^{N_e} \binom{R_i}{N_i}$ ¹. R_i is the remaining number of sites defined as $R_i = N_s$ when $i=1$; else $R_i = N_s - \sum_{j=1}^{i-1} N_j$. Noteworthy, the number of possible representations increases quickly with the number of sites and elements, and therefore, several realizations using large supercells are needed to obtain statistically meaningful results. The most computationally intensive way of tackling this issue is to use a large number of supercells, albeit there is not robust way to *a priori* ensure that the number and size of supercells are sufficient to achieve accurate statistical representation. A more refined

approach is so called special quasi-random structures (SQS) [51,52], which has been used for studying properties of HEAs [53]. Despite its more systematic conceptualization, SQS still requires to appropriate choice of supercell size and clustering size, which increases with the number of principal elements. The coherent-potential approximation (CPA) [54,55], in particular in its most-common practical implementations such as within the Korringa-Kohn-Rostoker (KKR) methods [56,57], or the exact muffin-tin orbitals (EMTO) [58], has been also frequently used approach to study HEAs [59]. Recently, it has been applied in an automated high-throughput framework to study a large compositional space of HEAs [60]. While CPA-based methods are highly promising to approximate a large number of materials properties, it is still a challenging task to obtain the large number of electronic and phonon properties required to consistently obtain the temperature-dependent electron-phonon (*e – ph*) coupling factor ($G_{e-\text{ph}}$), electronic specific heat (C_e) and electronic thermal conductivity (κ_e) for a given compositional space. For instance, it is quite computationally heavy to obtain phonon dispersion within CPA-based approaches for a large compositional space [61].

Thus, Samolyuk et al. have used a linear mixing scheme of the constant *e-ph* mass enhancement parameter (λ) of Ni, Cr, and Fe for that of their equi-molar binary alloys [62]. A less robust, yet extremely expedient approach is the virtual-crystal approximation (VCA) [63], which is conventionally applied a linear mixing scheme to atomic pseudo-potentials [64]. It offers a disordered mean-field limit approximation for configurational disorderliness as in HEAs. By construction, VCA is missing any short-ranged ordering, or details of local chemical environment. However, it is highly suitable when approximating *average* materials properties of disordered system such as $G_{e-\text{ph}}$, C_e and κ_e , which are commonly approximated by averaging over microscopic quantities. Despite its crude oversimplification, it has been shown that VCA is relative accurate when calculating elastic constant, simple-phase transformation, and thermodynamic functions of HEAs [65]. In particular, it can provide suitable tools when trend analysis throughout a composition space due to equally present systematic errors within it. The VCA approximation is used in this work to compute average electronic properties of HEAs including several elements in a wide range of compositions.

This work presents a first-principles investigation of electronic properties in MPE alloys at several molar compositions. The temperature-dependent $G_{e-\text{ph}}$, C_e and κ_e are calculated within fully first-principles approaches. There has been previous works [62,66–68] on elemental metals and binary alloys, partially carrying the electronic temperature effects. In this work, the underlying quantities such as λ , the Eliashberg function, the Fermi velocity, the plasmon lifetime and the electronic thermal conductivity are directly calculated for each electronic temperature point between 100 – 30000 K for each composition. Additionally, the influence of the electronic effects in an equimolar CoCrFeNi HEA is investigated under radiation environments within MD simulations incorporating the electronic effects using the *local* two-temperature molecular dynamics ($\ell^2\text{2T-MD}$) method [46,69]. For the first time, our work provides accurate first-principles electronic data for MPE alloys and shows the importance of these effects in radiation damage. Remarkably, we have found that neglecting these effects could lead to large overestimations of the FP population (up to ~ 20 – 25%) even at low PKA energies of 50 keV. An expedient model is developed to predict vacancy formation for the compositional space of Cr-Fe-Co-Ni. Temperature-dependent first-principles electronic, and phonon properties database, and MD defect-evolution database are made available in the repository at Ref. [70].

¹ Using the combination notation defined as $\binom{N_s}{N_1} = \frac{N_s!}{N_1!(N_s-N_1)!}$

2. Theoretical and computational methodology

2.1. Calculating first-principles electronic, and phonon properties

Let us now describe the relevant parameters of interest needed to quantify the electronic effects in multi-PE alloys. The temperature-dependent e – ph coupling factor G_{e-ph} is given by [71,72]

$$G_{e-ph} = -\frac{\pi \hbar k_B \lambda \langle \omega^2 \rangle}{g(E_F)} \int_{-\infty}^{\infty} d\epsilon \frac{\partial f(\epsilon, \mu, T_e)}{\partial \epsilon} g^2(\epsilon), \quad (1)$$

where k_B is the Boltzmann constant, $g(E)$, E_F , and μ are the electronic density of states (EDOS), the Fermi energy, and the chemical potential, respectively; $f(\epsilon, \mu, T_e)$ is the Fermi-Dirac distribution function. The product of λ and the mean square phonon frequency, $\lambda \langle \omega^2 \rangle$, is given by

$$\lambda \langle \omega^2 \rangle = 2 \int_0^{\infty} d\omega \omega \alpha^2 F(\omega), \quad (2)$$

with $\alpha^2 F(\omega)$ is the Eliashberg spectral function. The temperature-dependent electronic specific heat, C_e , is given by [72]

$$C_e = \int_{-\infty}^{\infty} d\epsilon (\epsilon - E_F) \frac{\partial f(\epsilon, \mu, T_e)}{\partial T_e} g(\epsilon). \quad (3)$$

The final component to describe the electronic properties of materials related to heat conduction, is the temperature-dependent thermal conductivity, κ_e , given by [37],

$$\kappa_e = v_F^2 \tau_p C_e, \quad (4)$$

where v_F , and τ_p are the Fermi velocity, and the plasmon lifetime, respectively, which are also implicitly dependent on the electronic temperature.

The three central quantities in Eqs. (1), (3), and (4) require accurate estimation of $g(E)$, E_F , λ and $\alpha^2 F(\omega)$, v_F and τ_p . Kohn-Sham density-functional theory (KS-DFT) [73–77] is almost-ubiquitous first-principles approach to calculate electronic structures of solids. Its perturbative extension, called the density-functional perturbation theory (DFPT) [78, 79], also provides an expedient approach for obtaining zero-temperature phonon properties. Despite rapid advancements in underlying algorithms, and computational resources, the KS-DFT-based implementations are severely limited in terms of system size and spatial complexity, in particular for metallic systems [49,50]. It is particularly challenging in the cases of HEAs, since it requires a large number of supercell simulations to achieve an accurate statistical representation configurational disorderliness. Virtual-crystal approximation (VCA) is an expedient approach to study multi-principles elements solids at the disordered mean-field limit [80]. Within VCA, the atomic pseudo-potentials [64] of constituent elements are linearly mixed to a single pseudopotential, representing a virtual atom [63].

In principle, DFT is an *absolute-zero-temperature* theory. However, it is worth to mention that there has been considerable work on extending it to capture thermal equilibrium at finite temperatures [81]. In the context of this work, the extreme electronic temperature are highly localized as it is generated by high-energy particles. Thus, the finite electronic temperature effects can be expediently included within a simple conceptual way through the smearing parameter around the Fermi level, representing T_e , in the case of metallic systems. With that in mind, $g(E)$ is expected to have a negligible T_e -dependence as it only affects occupancies of the electronic states at around the Fermi level as the practical DFT assign occupancies after optimizing the KS states. It is more suitable to include the possible effects of T_e through E_F as it does not require a large number of electronic band-structure simulations. The T_e -dependent E_F can be easily obtained using the zero-temperature electronic structure with little additional computational cost. We refer the reader to Refs. [82] and [83] for details on how to obtain λ and $\alpha^2 F(\omega)$, using DFPT. The T_e -dependence can be partially introduced by

setting the smearing parameter used for the double-delta integral during the e-ph coupling simulations.

Consistently, the averaged Fermi-velocity square, $\langle v_F^2 \rangle$, can approximately given by [84]

$$\langle v_F^2 \rangle = \frac{\left(\sum_m \int_{S_{Fm}} d\mathbf{k} \left| \frac{\partial E_{m,k}}{\partial \mathbf{k}} \right|^2 \right)}{\left(\sum_n \int_{S_{Fn}} d\mathbf{k}' \right)}, \quad (5)$$

assuming that the electronic bands have parabolic dispersions normal the Fermi surface. S_{Fm} , and $E_{m,k}$ are the partial Fermi surface, and the KS energy of the m – th metallic band, respectively. In practice, $\langle v_F^2 \rangle$ is calculated on a slab with a thickness of ΔE_{Fermi} using the in-house post-processing tool [85], available in Ref. [86]. It requires a well-converged electronic band structure on an extremely dense Brillouin-zone sampling. The T_e -dependence can be consistently included by setting $d_{\text{Fermi}} = k_B T_e$ [87]. We point out that Eq. (5) does not include the e – ph coupling effects, which can be introduced as the electron mass renormalization such as $v_F \rightarrow v_F / (1 + \lambda)$ [88].

Ignoring any impurity, the plasmon lifetime of a metallic solid can be expressed as the sum of the electron-electron (e – e) and the electron-phonon (e – ph) scatterings terms within Matthiessen's rule such as

$$\frac{1}{\tau_p} = \frac{1}{\tau_{e-e}} + \frac{1}{\tau_{e-ph}}. \quad (6)$$

The e – e term (in the Hz unit) can be estimated using the Fermi liquid theory at the absolute-zero temperature by [89–91]

$$\frac{1}{\tau_{e-e}} = \frac{me^4(E - E_F)^2}{64\pi^3 \hbar^3 \epsilon_0 E_s^{3/2} E_F^{1/2}} \left(\frac{2\sqrt{E_s E_F}}{4E_F + E_s} + \arctan \sqrt{\frac{4E_F}{E_s}} \right), \quad (7)$$

where m , e , \hbar , and ϵ_0 are the electronic mass, the unit charge, the reduced Plank's constant and the vacuum permittivity, respectively. The kinetic energy due to the Thomas-Fermi screening length $q_s = e\sqrt{g(E_F)/\epsilon_0}$ given by $E_s = \hbar^2 q_s^2 / (2m)$. By setting $(E - E_F) = k_B T_e$, the T_e -dependence can be consistently introduced alongside the T_e -dependent E_F . The second term in Eq. (10) is approximately given by [82,92]

$$\frac{1}{\tau_{e-ph}} = \frac{2\pi k_B \lambda T_e}{3}. \quad (8)$$

2.1.1. Computational details of first-principles simulations

First-principles simulations were performed using the Quantum ESPRESSO (QE) software [93,94] with the external thermodynamics thermo_pw package [95]. Fermi velocities were calculated using an in-house code available in Ref. [86]. The SG15 optimized norm-conserving Vanderbilt (ONCV) scalar-relativistic pseudo-potentials [96,97] (version 1.2) using the Perdew-Burke-Ernzerhof (PBE) exchange-correlation functional [98–100] were used for the four base elements (Cr, Fe, Co and Ni), as well as the additional elements (Al, Mn and Cu). Atomic pseudo-potential were used to obtain the virtual atoms representing MPEs alloys within VCA. The spin-polarization has been ignored to be consistent as the spin-polarization has not been yet implemented within the quasi-harmonic approximation [101] in the thermo_pw package. However, the relevant electronic and phonon properties are needed to approximate macroscopic quantities by averaging over the first Brillouin zone. Thus, while the local magnetic ordering may play a crucial role in phonon dispersions, it is expected to become less significant after averaging, in particular for HEAs [102–104].

The initial crystallographic information for the thermodynamically most-stable phases of the base elements was extracted from Ref. [105]. Cr and Fe have body-centered cubic (BCC) structures, while Co and Ni have hexagonal closed-packed (HCP) and face-centered cubic (FCC) structures. The FCC Ni structure was used as a template for the initial crystal structures for the HEAs. Variable-cell relaxation was performed

using a common high kinetic energy cutoff of 150 Ry on a $12 \times 12 \times 12$ Monkhorst-Pack-equivalent Brillouin zone sampling (MP-grid) [106], and the convergence for the total energies, the total forces, and the self-consistency were set to 10^{-7} Ry, 10^{-6} Ry· a_0^{-3} and 10^{-10} , respectively.

To practically mimic the extreme electronic temperatures of ~ 30000 K on irradiated surfaces, the temperature grid was divided into two parts such as a low temperature grid of $100 - 1000$ K with a step size of 100 K, and a high temperature grid of $3000 - 30000$ K with a step size of 3000 K. The electronic temperatures were consistently introduced a smearing parameters around the Fermi levels in all simulations. The first set of simulations were performed to obtain anharmonic thermodynamic properties were calculated for the low- T_e using the quasi-harmonic approximation [101] within the `thermo_pw` package on a shifted $12 \times 12 \times 12$ MP-grid for electronic structure simulations, and a $4 \times 4 \times 4$ MP-grid for phonon simulations. The e – ph mass enhancement parameters were calculated by following the procedure in Refs. [82] and [83] with a dense $36 \times 36 \times 36$ MP-grid for interpolation, and a converged $12 \times 12 \times 12$ MP-grid for electronic structure simulations, $4 \times 4 \times 4$ MP-grid for phonon simulations. Finally, the Fermi velocities were calculated using the in-house code starting from the band structures, calculated on a $36 \times 36 \times 36$ MP-grid. Temperature-dependent electronic, and phonon properties upto 3×10^4 K have been made publicly available in the repository at Ref. [70].

2.2. ℓ 2T-MD Methodology

The ℓ 2T-MD method, developed by Ullah and Ponga [46], provides computationally feasible and seamless approach to simulate the electronic effects in MD simulations within the two-temperature model. Considering a system with N_a atoms, each atom is provided with an electronic temperature variable. Let (T_i^e) denote the electronic temperature associated with the i – th atom in the system which can fluctuate locally depending on the local environments during a cascade even². At the same time, let us introduce a maximum electronic temperature T_{\max}^e representing an arbitrary upper bound to the electronic temperature of the system. On the basis of this maximum temperature, we can map the temperature field using the transformation $\theta_i = \frac{T_i^e}{T_{\max}^e}$ which maps $\theta_i \in [0, 1]$ interval.

According to Ullah and Ponga [46], the ℓ 2T-MD model electronic temperature evolution using the following master equation.

$$\begin{aligned} \frac{\partial T_i^e}{\partial t} &= \underbrace{\frac{G_{e-ph}}{C_e} T_{\max}^e (\theta_i^{\text{lat}} - \theta_i^e)}_{e-ph} \\ &+ T_{\max}^e \sum_{j \neq i}^{N_A} \underbrace{K_{ij} \left[\theta_j^e (1 - \theta_i^e) e^{\theta_i^e - \theta_j^e} - \theta_i^e (1 - \theta_j^e) e^{\theta_j^e - \theta_i^e} \right]}_{e-e} \end{aligned}$$

In Eq. (0) the time-evolution of T_i^e for each atom is influenced by the energy exchange energy between electrons surrounding the i – th atom (and denoted by (e – e)), and a coupling between electron and phonons (e – ph). K_{ij} is a material property that quantifies the rate of electronic energy exchange between electrons near two adjacent atomic sites. Interestingly, K_{ij} can be linked to well-defined properties obtained either from *ab-initio* simulations or experimental data and is going to be described below.

The term G_{e-ph} measures the e – ph scattering between electrons close to the Fermi level and phonons and determines how effectively the energy exchange between e – ph occurs. On the other hand, the term C_e

determines how much excess energy electrons can absorb. By definition, both of these terms are always positive for metals. A higher G_{e-ph} leads to more rapid energy exchange between e – ph, while a higher C_e allows to store more excess energy in the free electrons. When a sudden amount of energy is introduced in the system, there is a rapid rise in the lattice temperature (T_l^{lat}), which electrons around the Fermi level can partially absorb until the electronic and lattice temperatures reach equilibrium. We notice that $\theta_i^{\text{lat}} = T_i^{\text{lat}} / T_{\max}^e$ in Eq. (0) denotes a mapped local lattice temperature that is classically defined by

$$T_l^{\text{lat}} = \frac{2}{3k_B N_c} \sum_{j=1}^{N_c} \frac{1}{2} m_j v_j^2, \quad j \neq i \quad (9)$$

N_c is the number of atoms in a small cluster surrounding the i – th atom. The small cluster is defined within a cut-off radius, r_c , which is equal to the interatomic potential's cut-off used in MD [46]. m_j , and v_j are the atomic mass and the velocity vector of the j – th atom.

The pair-wise exchange-rate thermal coefficient K_{ij} for the electronic temperature can be determined by a long-wave analysis to well defined thermodynamics properties [46,69,107] and is given by

$$K_{ij} = \frac{2d\kappa_e}{C_e Z b^2} = \frac{2 d v_F^2 \tau_p}{Z b^2}, \quad (10)$$

where $d = 3$ is the system dimension, Z is the coordination number of the lattice without distortion, and b is the Burgers vector.

2.2.1. Computational details of classical molecular dynamics simulations

MD and ℓ 2T-MD simulations were performed using the Large-scale Atomic/Molecular Massively Parallel Simulator (LAMMPS) software [108], into which the ℓ 2T-MD have been implemented by Ullah and Ponga [46]. The ℓ 2T-MD routine was modified to allow G_{e-ph} , C_e , and κ_e to be updated with T_i^e . A binary search algorithm on a hook-up table was used to find the correct parameters range corresponding to T_i^e , while linear interpolation was used to interpolate the values corresponding to the exact T_i^e . The embedded atom model (EAM) potential by Farkas and Caro [109] was used as the interatomic potential as it can model HEA of Co, Cr, Fe and Ni and was used previously in literature for modeling radiation damage for HEA [28,110]. The electronic stopping was incorporated in the model through electron stopping fix in LAMMPS [111,112]. The stopping-power values were calculated using the Stopping and Range of Ions in Matter (SRIM) software [113] with a minimum cut-off energy of 10 eV. For the sake of completeness and robustness, the minimum cut-off energies of 1, 5 and 10 eV were tested for CrFeCoNi within the ℓ 2T-MD. The short-range interactions were modified using a ZBL potential [114] to prevent atoms from getting too close during the displacement cascades. The ZBL potential was smoothly linked to the EAM pair potential for distances between 0.05 nm and 0.18 nm. This procedure does not affect the equilibrium properties.

An initial cubic simulation cell with a dimension of $L = 34$ nm was used to fill using a generic crystal with a lattice parameter of $a = 0.363$ nm with a total number of atoms of 3,538,944. This cell size ensured that the radiation-induced damage was contained within the simulation cells' boundaries. Periodic boundary conditions were employed in all three directions for all simulation cells. The initial simulation cells of CoCrFeNi were obtained by randomly placing Co, Cr, Fe and Ni on the atomic sites. We performed the following test to validate the random generation to ensure the correct statistical sampling. First, 512 random generations were performed in smaller samples containing ~ 500 atoms. These samples were relaxed using molecular statics and subjecting them to zero pressure. Then, the energy per atom (~ -4.1232 eV/atom) and its standard deviation (~ 4 meV/atom) were measured. These samples indicated a distribution close to a Gaussian of energies after minimization, as shown in the Supplementary Materials (SM) Fig. S1.

² We point out that the subindexes i and j are used in the ℓ 2T-MD method to denote different atomic sites and should not be confused with traditional notation within the DFT formulations for different orbitals.

Subsequently, nine large cells involving 3,538,944 atoms were relaxed under the same conditions, and their average energy (~ -4.1229 eV/atom) and standard deviation were also obtained. The difference between average energies was less than 1 meV/atom, indicating a large number of chemical environments are simulated in the large sample. The energy levels correspond to the average values of the 512 different realizations suggesting proper sampling of the chemical environments.

Then the simulation cells were subjected to energy minimization at $T = 0$ K using the Polak-Ribière conjugate gradient algorithm [115]. Subsequently, an initial temperature of $T = 300$ K was given to the atoms, and the system was relaxed for 30 ps using the Nosé - Hoover thermostat to relax the hydrostatic pressure to zero. The same energy minimization and relaxation procedures were used for the Ni simulation cells.

Cascade events were initiated by randomly choosing a primary knock-on-atom (PKA) located at the center of the simulation cells. The PKA was given a random velocity vector corresponding to recoil energy of 50 keV in an NVE ensemble. For the ℓ^2 T-MD simulation, the average lattice and the average electronic temperatures (T_{lat} , and T_e , respectively) were initially set at $T = 300$ K before energizing the PKA. A variable time step was used with a maximum time step of ≤ 0.01 fs for the cascade simulations to limit the maximum distance for every time-step moved by the PKA atom to 0.005 Å. At each MD step, between 10 to 15 T_e integration time-steps of Eq. (0) were performed. The total time of the cascade simulations was about 32 ps, which was sufficient for the FPs to reach steady states. Each cascade simulation was repeated ~ 20 times with different random PKA directions and HEA structures to ensure sufficient statistical representation. To ensure this, the mean values of the total numbers of defected atoms (N_{def}) and Frenkel pairs (N_{FP}) was analyzed for the randomly selected subsets of the cascade simulations with respect to the number of simulations, shown in Fig. S13 and Fig. S14, respectively. Our analysis indicates that the total number of cascade simulations for each case reaches to convergence within $\pm 5\%$ accuracy of the overall mean value of all available simulations for each case.

The common-neighbor analysis (CNA) [116] was used to identify formations of defect clusters. The Ovito software was used for visualization of the defect structures [117], and the DXA algorithm was used for dislocation loops analysis [118]. Finally, the Wigner-Seitz defect analysis was performed to determine the vacancies and the self-interstitial atoms (SIA) using the Ovito software.

The related database of defect evolutions in Ni, and CrFeCoNi within the conventional MD, and the ℓ^2 T-MD has been made publicly available in the repository at Ref. [70].

3. Results and discussion

We start with thermodynamic and mechanical stability assessments

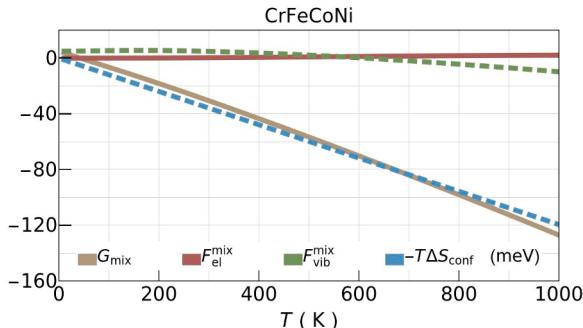


Fig. 1. Temperature dependent mixing Gibbs free energy (G_{mix}) for CrFeCoNi in RSS. Mixing electronic, and vibrational Helmholtz free energies ($F_{\text{el}}^{\text{mix}}$ and $F_{\text{vib}}^{\text{mix}}$, respectively), and the configurational-entropy contribution ($-T\Delta S_{\text{conf}}$) also shown in the plot. See SM for calculations details.

of our base HEA (CrFeCoNi) and its PEs. The mixing Gibbs free energy (G_{mix}) is an ubiquitous indicator for thermodynamic stability [119]. In Fig. 1, the mixing Gibbs free energy (G_{mix}) and the individual contributions to it are shown up to 1000 K. The configurational-entropy contribution is the predominant term, leading to thermal stability at a low temperature. At the same time, the mixing electronic and the mixing vibrational Helmholtz free energies ($F_{\text{el}}^{\text{mix}}$, and $F_{\text{vib}}^{\text{mix}}$, respectively) are negligible (see the SM for the details to calculate the free energies, and the configurational entropy). Addition to the thermodynamic stability, the elastic and dynamic stability is crucial to assess the mechanical stability. The elastic stability is assessed using the Born-Huang-stability criteria [120,121] (see the SM for the necessary and sufficient condition for cubic symmetry). The dynamic stability is assessed by analyzing phonon dispersions [122]. CrFeCoNi is both elastically stable according to the Born-Huang-stability criteria and dynamically stable as it has neither negative nor soft phonon modes [122].

In Fig. 2, $G_{e-\text{ph}}$, C_e , and κ_e are depicted for the four pure elements, and their equimolar FCC RSS. $G_{e-\text{ph}}$ exhibits quite similar trends for CrFeCoNi and the pure elements, exponentially vanishing with the increasing temperature. The integral term in Eq. (1) predominantly sets this trend when the individual terms are further analyzed as shown in Figs. S2 and S3. However, the non-integral terms for each system roughly average to the same order and determine magnitudes of $G_{e-\text{ph}}$. It becomes in order of 1 at around 500 K, indicating that electrons become too fast for e – ph scattering. On the other hand, C_e almost-linearly increases with the increasing T_e . This results to a rapid $G_{e-\text{ph}}/C_e \rightarrow 0$ for T_e above 500 K. This indicates that there will be very little energy transfer from electrons to lattice when $T_e \gg T_{\text{lat}}^{\text{eq}}$. On the other hand, despite also decreasing κ_e/C_e ratio, there will still be energy dissipation, mediated solely by electrons. This scenario is desirable to keep FPs formation by dissipating excess energy among electrons while avoiding further energizing the lattice.

Comparing C_e of CrFeCoNi with the pure elements, we observed that CrFeCoNi has a higher C_e , hinting that electrons have a better capacity to absorb energy compared to the pure metals. This effect could be important in radiation environments as the plasmons take on more thermal energy, which is removed from the lattice and thus could result in less FP formation. At lower temperatures, Cr exhibits higher κ_e compared to other PEs and CrFeCoNi, while CrFeCoNi, Co, and Ni performs better at higher electronic temperatures (i.e., $T_e \gtrsim 6000$ K). The trends in κ_e are predominantly determined by v_F , portrayed in Figs. S2 and S3, as well as λ as it renormalize v_F by including e – ph coupling effects. This effect leads to remarkable poor performance for Fe as it has the slowest v_F with the largest λ . Despite its not-so-superior κ_e when compared to those of the PEs, CrFeCoNi has a much higher C_e . It leads to a much smaller $K_{ij}\alpha = v_F^2\tau_p$, indicating that while its electrons could hold more energy for the same electronic temperature, they are less effective in dissipating it compared to the PEs. In summary, CrFeCoNi is expected to absorb excess lattice energy more effectively via e – ph coupling compared to the PEs, while less effective to dissipate it via e – e coupling except for Fe.

3.1. Compositional space of non-equimolar Cr-Fe-Co-Ni random solid solutions

Higher $G_{e-\text{ph}}$ and C_e are the key factors for a superior radiation-damage resistance in HEA. Thus, a potential strategy to improve radiation damage properties is to tune molar fractions of PEs to further improve these properties. We investigate the compositional space of the Cr-Fe-Co-Ni RSS. For a systematic yet feasible investigation, we vary each PE at a time on a molar-fraction grid of $x = [0, 0.05, 0.10, 0.15]$ while keeping the remaining three elements equimolar among themselves. The $x = 0$ cases are the equimolar 3-PFs cases; however, the non-CrFeCoNi cases are called the non-equimolar cases for simplicity. By varying each PE one by one, the individual effect of each PE can be

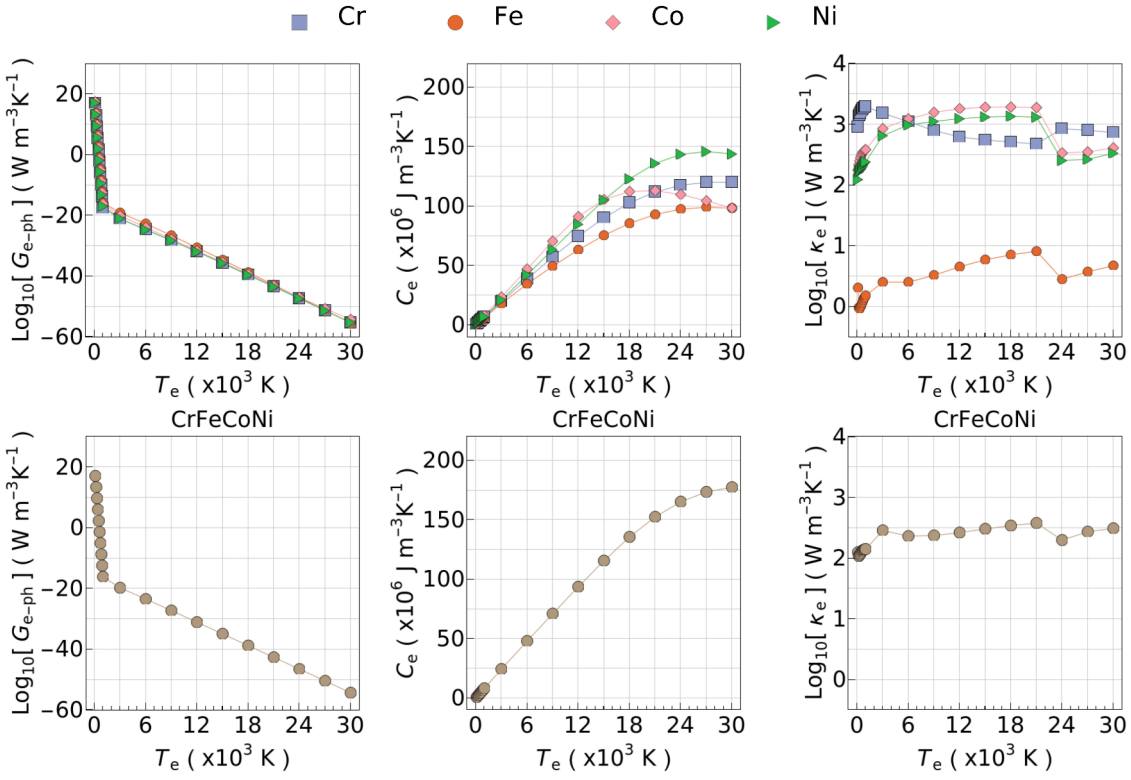


Fig. 2. Temperature dependence of the e – ph coupling factor (G_{e-ph}), the electronic specific heat (C_e), and the electronic thermal conductivity (κ_e) of the base PEs, and the FCC CrFeCoNi.

partially assessed, although reducing a single PE automatically increases the molar fraction of the remaining three.

The first step is to assess the relative stability of the non-equimolar RSS. In Fig. 3, the Gibbs free energy differences (ΔG) of the RSS compared to the CoCrFeNi are illustrated up to 1000 K. Reducing Cr or Fe leads to thermally less stable compositions by increasing G while reducing Ni has an opposite effect. Reducing the molar-fraction of Co has a less significant effect on the thermal stability, and this is consistent with previous studies carried out in five PE alloys [21]. At room temperature (300 K), a reduction up to 20% of Cr or Fe, or a reduction of Co only leads to ΔG in the order of 1 meV, which is in the order of the accuracy of the practical DFT simulations. Reduction of Ni already leads to better thermal stability; thus, it is thermally more favorable in any case. The non-equimolar RSS are also elastically stable according to the Born-Huang-stability criteria. They are also dynamically stable except for CoCrFe ($Ni_x(CoCrFe)_{1-x}$ for $x = 0$) as it has negative phonon modes at around the X high-symmetry point in the first Brillouin zone of the primitive FCC unit cell.

In Fig. 4, dimensionless ratios \bar{G}_{e-ph}^x , \bar{C}_e^x and $\bar{\kappa}_e^x$ for non-equimolar compositions are shown to assess their relative performance in dissipating excess energy. The dimensionless ratios are computed as the ratio of G_{e-ph} , C_e and κ_e of the non-equimolar RSS to those of CoCrFeNi. Reducing Cr concentration (first column in Fig. 4) quickly worsens G_{e-ph} and C_e starting at around the room temperature. It indicates that the lower Cr concentration can lead to less effective energy exchange between e – ph, shown to play a crucial role in promoting defect recombination and reducing defect clustering. Reducing Fe or Co concentrations (central columns in Fig. 4) have subtle effects on G_{e-ph} , C_e and κ_e . On the other hand, a 25 – 50% reduction of Cr significantly improves purely electronic heat dissipation, hinted by much higher κ_e . However, the comparative analysis carried out later on in Section 3.3 for Ni and CrFeCoNi indicates that the e – e term in Eq. (1) has a lesser effect on the defect evolution. At the lower temperatures ($T < 1000$ K) (the inset figures in Fig. 4), lower Ni concentrations improve G_{e-ph} with a less

significant loss in C_e . Unlike Cr, lower Ni concentrations drastically worsen κ_e ($\sim 50\%$) at lower temperatures. The composition-dependent relative changes in G_{e-ph} are determined mainly by ratios of the electron-phonon mass enhancement parameters (λ), while the ratios of the Fermi velocities primarily determine the general trends in κ_e (v_F), shown in Figs. S4-S7.

3.2. Equimolar additions of Al, Mn, or Cu

Another strategy to tailor the electronic and phonon parameters is to add other elements rather than exploring non-equimolar compositions. In Fig. 5, the relative thermal stabilities of equimolar AlCrFeCoNi, CrMnFeCoNi (also known as Cantor alloy), and CrFeCoNiCu are shown with respect to CrFeCoNi. While introducing Al or Mn leads to better thermal stability, CrFeCoNiCu becomes less thermally stable. However, it is still thermally stable in its own merit as indicated its mixing Gibbs free energy, shown in Fig. S11 using the thermal data for the elemental Cu from Ref. [87]. While all three RSS are elastically stable according to the Born-Huang-stability criteria, only CrMnFeCoNi and CrFeCoNiCu are dynamically stable as AlCrFeCoNi has negative phonon modes at around L high-symmetry point in the first Brillouin zone of the primitive FCC unit cell.

In Fig. 6, the relative performance of the electronic ($\bar{G}_{e-ph}^{Al/Mn/Cu}$, $\bar{C}_e^{Al/Mn/Cu}$ and $\bar{\kappa}_e^{Al/Mn/Cu}$) properties compared to CrFeCoNi are shown. The very first observation is that the addition of Al drastically increases G_{e-ph} ³, as well as substantially increases C_e and κ_e by more or less ~ 2 times compared to those of CrFeCoNi. On the other hand, the addition of Mn has almost-no effect on G_{e-ph} , C_e , or κ_e . Finally, the addition of Cu worsens G_{e-ph} and improves $\kappa_e \sim 1.5$ times while almost no effect on C_e .

³ Note that the scale for Al is represented at the left of the plot and is several times higher than for the other two elements.

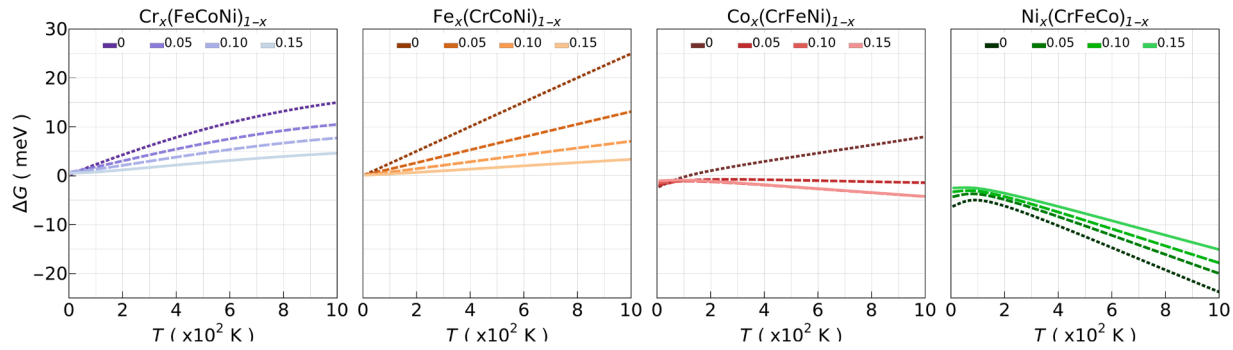


Fig. 3. Temperature dependent Gibbs free energy differences (ΔG) for non-equimolar compositions compared to the CrFeCoNi random solid solution.

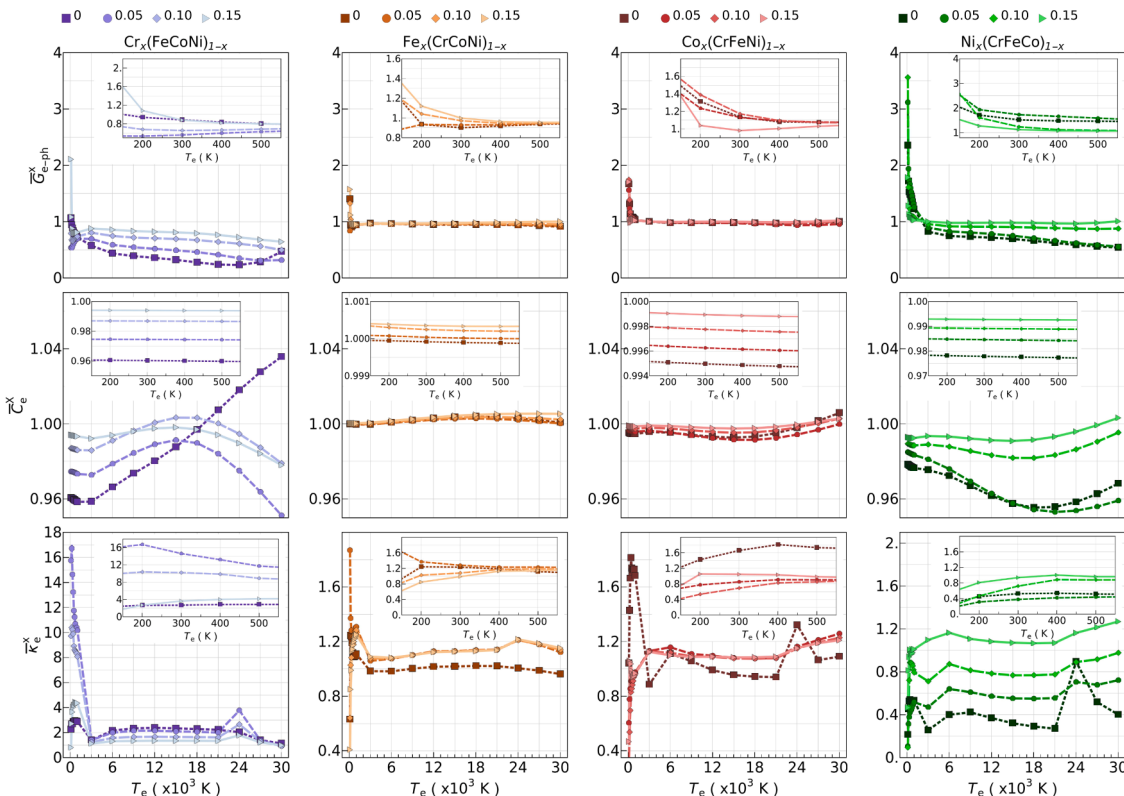


Fig. 4. Temperature dependence of the electronic property ratios for non-equimolar compositions compared to CrFeCoNi. The e – ph coupling factor ratio ($\bar{G}_{e-\text{ph}}^x$), the fractional electronic specific heat (\bar{C}_e^x), and the fractional electronic thermal conductivity ($\bar{\kappa}_e^x$) fractions for non-equimolar random-solid solutions compared to CrFeCoNi.

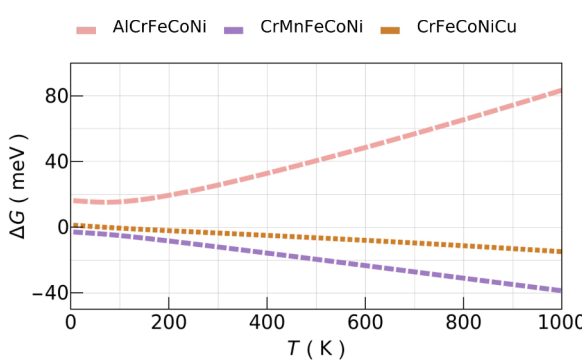


Fig. 5. Temperature dependent Gibbs free energy differences (ΔG) for equimolar AlCrFeCoNi, CrMnFeCoNi, and CrFeCoNiCu compared to the CrFeCoNi.

The drastic increase in $G_{e-\text{ph}}$ of AlCrFeCoNi is mostly due to the integral term in Eq. (1), as well as higher $\lambda(\omega^2)$ and lower $g(E_F)$, as displayed in Figs. S8 and S9. The higher λ values can be mainly attributed to lower averaged mass as phonon modes are normalized with the average mass of the unit cell. On the other hand, introducing Mn, which is *most-alike* to CrFeCoNi in terms of its averaged atomic mass and VEC, has the most negligible effects on the EDOS and phonon DOS (PDOS); thus, $G_{e-\text{ph}}$ is almost identical except at the very low temperatures. In the case of CrFeCoNiCu, the lower λ alongside negligible increment in other significant terms in Eq. (1), shown in Fig. S12, leads to a lower $G_{e-\text{ph}}$.

In the case of C_e , the EDOS is the principal figure of merit, as imposed by Eq. (3) (in particular, due to $\mu \approx E_F$). When comparing the EDOS of the four systems in the top-right panel of Fig. S8, the EDOS of CrFeCoNi, CrMnFeCoNi, and CrFeCoNiCu are pretty similar. On the other hand, AlCrFeCoNi has lower yet more spread-out EDOS, leading to higher C_e . With that in mind, the higher κ_e of AlCrFeCoNi is due to its higher C_e , as

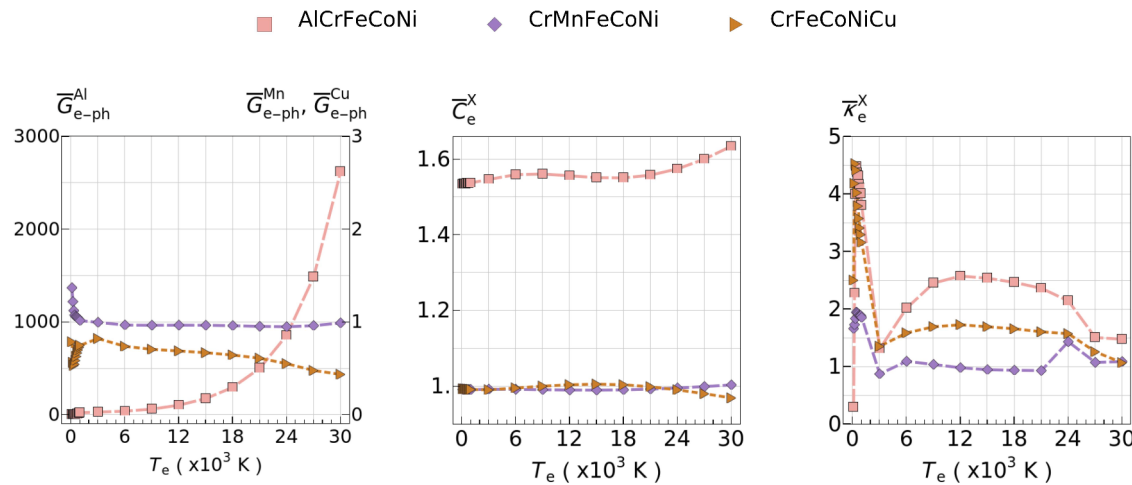


Fig. 6. Temperature dependence of the electron-phonon coupling factor ($G_{e-\text{ph}}$), electronic specific heat (C_e), and electronic thermal conductivity (κ_e) fractions of AlCrFeCoNi, CrMnFeCoNi, and CrFeCoNiCu compared to CrFeCoNi. Note that $G_{e-\text{ph}}^{\text{Al}}$ scale is shown at the left of the plot.

well as its faster free electrons despite shorter-living, shown in Fig. S9. Without any contribution from C_e , the almost-identical κ_e of CrMnFeCoNi is due to counter-balancing of changes in v_F and τ_p . On the other hand, CrFeCoNiCu has faster as well as longer living plasmons, leading to slightly higher κ_e . As τ_p is inversely proportional to λ via Eq. (8), which is the predominant term in Eq. (10), a higher λ leads to a lower τ_p . Similarly, v_F is renormalized by $(1 + \lambda)$, a higher λ lower it. However, a steeper band dispersion can compensate for this reduction, as in the case of AlCrFeCoNi.

When introducing additive elements, the relative changes in $G_{e-\text{ph}}$ and κ_e are determined by both electronic and phonon properties, while C_e is purely electronic. In the case of κ_e , it is also dependent on fine details of electronic band dispersion and Fermi surface.

3.3. Benchmark: Defect evolution in Ni and CrFeCoNi

Despite its relatively well-scalability, accurate MD simulations are still computationally challenging, particularly to achieve a reasonable statistical representation of HEAs. Thus, the elemental Ni and CrFeCoNi are chosen as the benchmark cases to simulate the defect evolution.

We start by analyzing the time evolution of the average temperatures depicted in Fig. 7. For both materials, the initial average T_{lat} spike to ~ 408 K from the initial 300 K due to the additional kinetic energy of PKA. We also notice that for the ℓ 2T-MD simulations, the average electronic temperature also shown in Fig. 7 remains at 300 K at $t = 0$ ps. For classic MD and ℓ 2T-MD simulations, the lattice temperature showed a quick dip at around ~ 0.25 ps in T_{lat} (listed in Table S2) as the PKA transfer energy to the surrounding atoms and rapidly generated defects. After that, the lattice temperature quickly stabilizes near a steady-state value that is very similar for MD simulations (355 K and 356 K for Ni and CoCrFeNi, respectively).

On the other hand, examining the ℓ 2T-MD simulations, we observed a much different behavior. For those simulations incorporating the electronic effects, the lattice temperature continuously reduced its value as time went by, whereas the electronic temperature monotonically increased. These two temperatures eventually reached equilibrium (at 334 K and 332 K for Ni and CoCrFeNi, respectively) at around $t = 32$ ps. We also observed that the standard deviation of these values was around ± 2 K, illustrating a very robust statistical response of the multiple replicas used in the study. The analysis of the average temperature of the system with time suggests subtle differences between Ni and CoCrFeNi, and thus, it is beneficial to investigate the evolution of the maximum temperatures during the simulations.

Fig. 8 compares the maximum local lattice and electronic

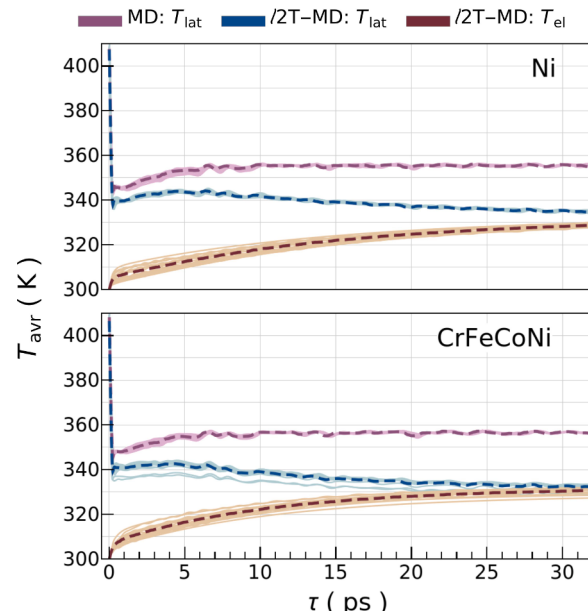


Fig. 7. Time evolution of the average lattice (T_{lat}) and electronic (T_{el}) temperatures for Ni and CrFeCoNi within the conventional MD and ℓ 2T-MD for a 50 keV PKA. The mean values of the repeated eight simulations are shown with dashed lines.

temperatures during the cascade simulations within ℓ 2T-MD simulations. At first glance, we observed that the peak of lattice temperature was the same for both materials, whereas the peak for the electronic temperature was different (see insets in Fig. 8). The time to reach the maximum electronic temperature (~ 0.05 ps) is comparable with plasmon lifetime τ_p and could hint at ballistic electronic heat conduction near the PKA for both materials. While ballistic heat conduction is neglected in the electronic subsystem, it is considered through the explicit integration of the equation of motion in the lattice. We point out that the ℓ 2T-MD implementation allows for second sound simulations, and a computational implementation is provided in Refs [69, 107]. We also observed for CoCrFeNi several oscillations in the maximum electronic temperature, hinting at local plasmon excitations during the PKA trajectory. As a result, and considering that the width of the peak was much longer for the CoCrFeNi compared to Ni, the lattice temperature dropped faster for CoCrFeNi than Ni. These facts hint at a better energy

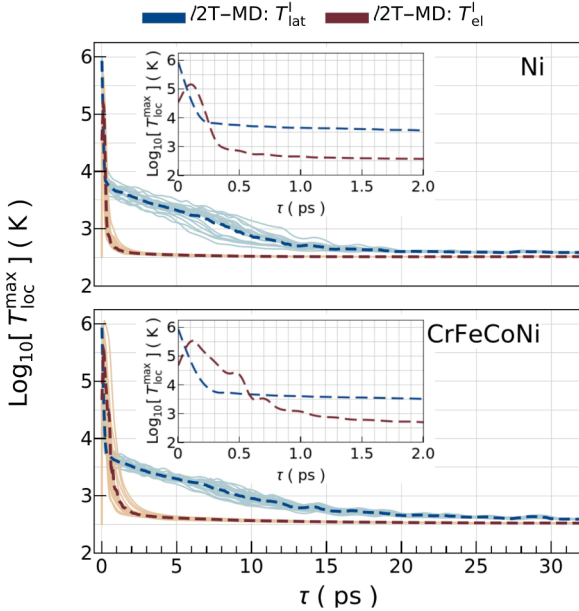


Fig. 8. Time evolution of the maximum local lattice temperatures (T_{lat}^l), electronic temperatures (T_{el}^l) of Ni and CrFeCoNi within the ℓ 2T-MD for a 50 keV PKA. The mean values of the repeated simulations are shown with dashed lines.

exchange between e – ph for CoCrFeNi compared with the pure metal. Indeed, the energy exchange between electrons and phonon is more significant in the case of CrFeCoNi as indicated more prolonged survival of T^e before reaching steady temperatures (at around 30 ps) compared to those of Ni, reaching steady temperatures at around 15 ps.

To better understand this energy exchange, Fig. 9 shows a graphical comparison of the local electronic properties between CrFeCoNi and Ni for the first $t = 2$ ps using the maximum electronic temperature. Remarkably, the ratio between $G_{e-\text{ph}}$ for CrFeCoNi and Ni is much greater than one below $t = 0.5$ ps, and eventually converged to two; suggesting a much faster exchange of thermal energy from the lattice to the electrons. Moreover, C_e is about 20% greater for CrFeCoNi compared to Ni although some variations are observed below $t = 0.5$ ps. Only the thermal conductivity of the high entropy alloy is less than Ni (about 70% of Ni), but it seems to have a much less critical impact on the thermodynamics behavior of the two subsystems.

3.3.1. Electronic effects in defect formation and recombination

Having analyzed the evolution of the electronic and lattice temperatures during the simulations, we now investigate the impact on defect formation when electronic effects are included. Fig. 10 depicts the time evolution of the defected atoms and FP in the simulations. Defected

atoms are defined as those atoms that do not belong to the FCC lattice. Qualitatively, the trends are very similar for defected atoms and FPs. An initial high-peak was observed at the earlier stages of the simulations, i.e., $\tau_{\text{def}}^{\max} = 0.31$ ps (listed in Table 1). A monotonic decay of defected atoms and FP followed until the number stabilized after $\tau^{\text{steady}} = 8 - 10$ ps. The number of defected atoms and FP was higher for all MD simulations compared to the ℓ 2T-MD simulations, and also for Ni compared to CoCrFeNi (cf. $N_{\text{def}}^{\text{steady}}$ and $N_{\text{FP}}^{\text{steady}}$ in Table 1 columns one and two, and three and four). At the initial stages of the cascade events, the steep decrease in T_{lat} leads to a rapid defected-atom generation as indicated by the sharp increase in the total number of defected atoms (N_{def}) in Fig. 10. The reduced number of FP compared to defected atoms indicates that during the early stages of the PKA, some defects form FP while some are only partially defected due to lattice distortions or recombine quickly due to the high local thermal energy. Nevertheless, besides reducing significantly after a few ps, FPs reached steady-state for all simulations after ~ 10 ps.

As shown in Table 1 the trends are analogous as the number of defected atoms with more FP for MD compared to ℓ 2T-MD and for Ni to CoCrFeNi. Interestingly, comparing the FP at the end of the simulations, a difference of $\sim 26\%$ was observed for Ni, and this is comparable with previous studies for pure metals [43–46]. Difference can be attributed to the temperature dependence implemented in our work compared to previous ones, where usually C_e and κ_e are modeled as a linearly dependent on T_e . However, as shown in Fig. 2, this is only true for moderate temperature ranges and both quantities saturate at high temperatures. Comparing the FP for CoCrFeNi, the incorporation of electronic effects resulted in 105 ± 4 FPs, whereas classical MD showed 126 ± 8 , or a difference of 20% between the two approaches. The significantly higher $G_{e-\text{ph}}$ of CrFeCoNi compared to that of Ni, shown in Fig. 9, significantly promote higher defect recombination, leading to lower FPs at steady-state.

It is evident from Fig. 10 that the electronic effects shorten the time scale to reach the steady states FPs. Thus, we conclude that the electronic effects play a more critical role in determining the final number of FPs after the PKA, and these effects are more critical than those made by the elastic distortions present in high-entropy alloys. To better explain this finding, we computed the SIA (s_f^l) and vacancy formation (v_f^l) energies in the HEA and compared to Ni and these results are shown in Fig. S15 and Fig S16. and listed in Table S3. For instance, the vacancy formation energy in CoCrFeNi has a Gaussian distribution owing to the elastic distortions. However, when analyzed on average, we observed that the formation energy $v_f^l \approx 1.64$ eV which is very close to one in Ni, $v_f^l = 1.56$ eV. These small differences suggest that the energetic cost of generating a vacancy is not strongly affected by the elastic distortions and thus, cannot drastically reduce FPs formation during the PKA event.

These findings are in line with previous results obtained by Deluigi et al. [28] where the effect of the elastic distortions was investigated and

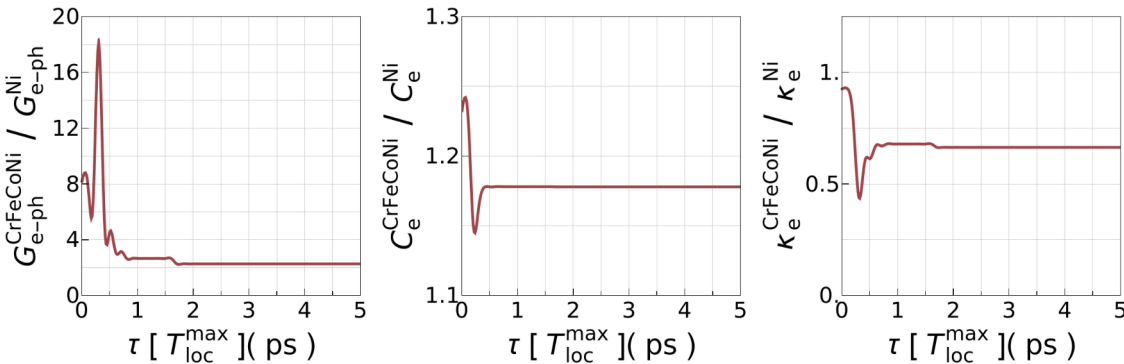


Fig. 9. Time evolution of the e – ph coupling factor ($G_{e-\text{ph}}$), the electronic specific heat (C_e), and the electronic thermal conductivity (κ_e) ratios between Ni and CrFeCoNi.

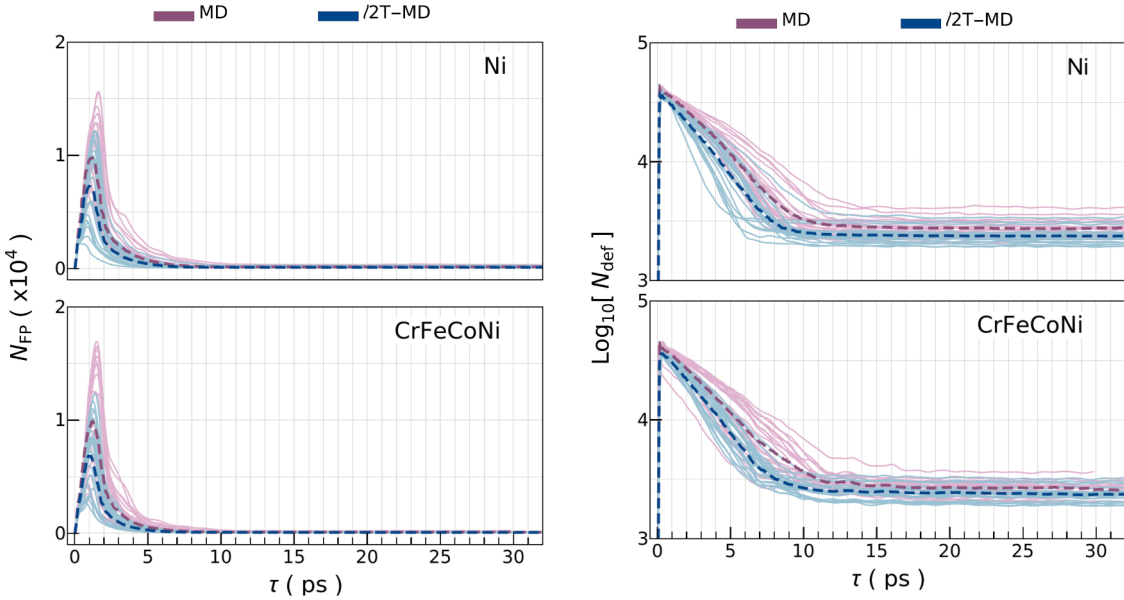


Fig. 10. Time evolution of the total numbers of defected atoms (N_{def}) and Frenkel pairs (N_{FP}) in Ni, and CrFeCoNi within the conventional MD and the ℓ 2T-MD simulations for a 50 keV PKA. Each simulation was repeated eight times to ensure sufficient statistical representation of cascade events.

Table 1

The mean values and standard error (in parenthesis) of the maximum number of defected atoms at the peak of the thermal spike (N_{def}^{\max}), at steady state ($N_{\text{def}}^{\text{steady}}$), their corresponding times (in Picoseconds units) (τ_{\max} , and τ_{steady} , respectively), and the number of Frenkel pairs ($N_{\text{FP}}^{\text{steady}}$), obtained within the conventional MD and the ℓ 2T-MD simulations for a 50 keV PKA.

Ni		CrFeCoNi		
MD	ℓ 2T-MD	MD	ℓ 2T-MD	
N_{def}^{\max}	40,587 (402)	37,105 (397)	42,066 (345)	37,441 (412)
τ_{def}^{\max}	0.31 (0.01)	0.31 (0.01)	0.31 (0.02)	0.30 (0.01)
$N_{\text{def}}^{\text{steady}}$	2877 (102)	2467 (83)	2754 (80)	2483 (82)
$\tau_{\text{def}}^{\text{steady}}$	12.53 (0.54)	11.70 (0.56)	15.13 (0.61)	14.65 (0.74)
$N_{\text{FP}}^{\text{steady}}$	165 (15)	131 (11)	126 (8)	105 (4)
$\tau_{\text{FP}}^{\text{steady}}$	9.64 (0.50)	9.43 (1.10)	9.19 (0.31)	9.72 (0.64)

compared to an equivalent mean-field discrete sample. Noteworthy, Deluigi *et al.* [28] concluded that the elastic distortion plays a minor role in the generation of FP during low energy PKA events. Even though these authors did not include electronic thermal effects, we observe similar trends here. These results illustrate the importance of the electronic effects in MD and justify their inclusion besides increasing the simulations' computational cost.

For the sake of gaining further insight, the cascade simulations for CrFeCoNi within the ℓ 2T-MD were repeated for the minimum cut-off energy for the electronic stopping, listed in Table S1. The minimum cut-off energies (1, 5, and 10 eV) do not have any significant effects on the numbers of the defected atoms and/or Frenkel pairs.

3.3.2. Electronic effects in defect clustering

Another important factor in comparing the classical MD and ℓ 2T-MD simulations is the size of the defected cluster resulting after the cascade simulations. To this end, we graphically represented the cluster size (as denoted by the defected atoms in different defect clusters in the simulations) for twenty clusters as shown in Fig. 11 and also visualized in Fig. S17. Again, results for MD and ℓ 2T-MD for Ni and CoCrFeNi are compared.

Ni generates larger defect clusters without the electronic effects, as much as ~ 1.5 times larger ones than those of CrFeCoNi. When the

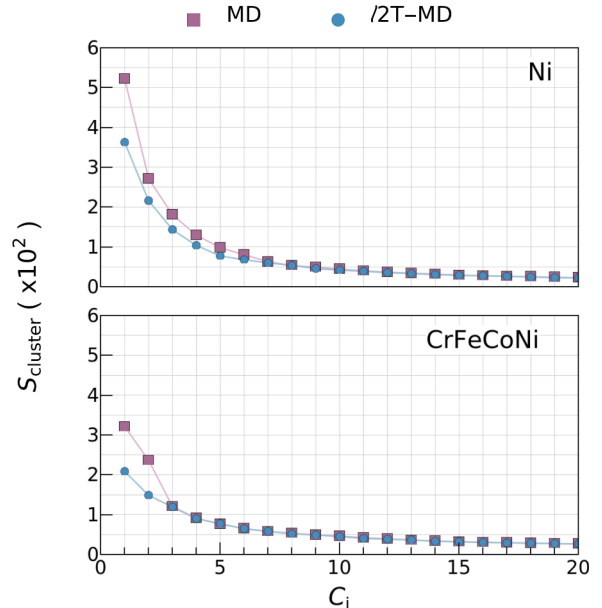


Fig. 11. Comparison of the defect cluster size (S_{cluster}) for each cluster in descending order of size (C_i) in Ni, and CrFeCoNi within the conventional MD and the ℓ 2T-MD simulations for a 50 keV PKA.

electronic effects are included, this ratio rises to ~ 2 . Smaller S_{cluster} in CoCrFeNi compared to Ni can be attributed to better energy exchange between e – ph ($G_{e-\text{ph}}$) and heat capacity ($C_{e-\text{ph}}$). Remarkably, the lower values of thermal conductivity ($\kappa_e^{\text{CrFeCoNi}}$, displayed in Fig. 9) of the high entropy alloy compared to Ni play a much more modest role in determining the FPs and cluster size. Despite different lattice distortion, the electronic effects reduce $S_{\text{cluster}}^{\max}$ by $\sim 34\%$ in CrFeCoNi compared a reduction of $\sim 30\%$ in Ni.

Fig. 12 exhibits the steady-state fractions of FPs per principal elements are shown for CrFeCoNi. Even though at the initial stages of the cascade simulation, the FPs are equally distributed in all elements (not shown in the figure), the distribution quickly shifts and reaches the distribution as illustrated in Fig. 12. As clearly portrayed in the graphical

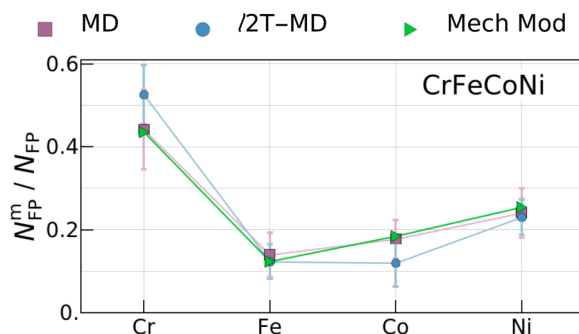


Fig. 12. Fractional FPs of the principal elements in CrFeCoNi after a 50 keV PKA obtained with MD (purple), the $\ell/2T$ -MD (blue). A simplistic mechanistic model results are also included (green). (For interpretation of the references to colour in this figure legend, the reader is referred to the web version of this article.)

representation, Cr disproportionately forms more FPs while Fe and Co contribute less to the total FPs population. This disparity in the FPs proportion is simply due to lower vacancy and SIA-formation energies of Cr compared to other PEs, as shown in Fig. S15 and Fig. S16. The different FPs fractions open up the question of exploring the compositional space of CrFeCoNi for tuning the electronic and phonon properties to improve the radiation-damage resistance.

To better explain the distribution of FPs in a steady-state, let us use the available information and a simple mechanistic model to predict these fractions. This prediction is insightful because it can help guide non-equimolar HEAs' design for radiation resistance. First, let us define the average vacancy and SIA formation energy denoted as $\bar{v}^f = \sum_i^{N_e} x_i v_i^f$ and $\bar{s}_f = \sum_i^{N_e} x_i s_i^f$, respectively, with x_i the atomic molar fraction of the HEA. At the same time, let us now assume that the di-vacancy and di-SIA formation energies can be computed. Next, the probability that a FP formation of a given element is given by the following biased probability, $\rho_i = \exp(-\Delta v_i^f / \bar{v}^f - \Delta s_i^f / \bar{s}_f - \Delta v_i^{2f} / \bar{v}^{2f} - \Delta s_i^{2f} / \bar{s}^{2f})$. In the biased probability function, the arguments Δ are taking with respect to the average value, i.e., $\Delta v_i^f = \bar{v}^f - v_i^f$. The relative changes in formation energies shift the probabilities to generate more FPs of those elements with lower than the average values. Next, the fraction of FPs can be obtained by using the atomic molar fraction of the HEA considered, i.e., $x_i^{FP} = x_i \rho_i$. Using the values provided above and the described model, we obtained for an equimolar HEA the following concentration of FP defects by elements, $\text{Co}^{FP} = 0.185$, $\text{Cr}^{FP} = 0.436$, $\text{Fe}^{FP} = 0.124$, and $\text{Ni}^{FP} = 0.255$, which is pretty approximate to the values found by MD while some discrepancy for Co and Cr is seen for $\ell/2T$ -MD. Thus, while the number of defects can be estimated well with the available models [123], the proposed procedure can be used to estimate the FPs distribution per element.

4. Conclusion

This work presented a systematic study of temperature-dependent electronic and phonon properties crucial during defect formation in HEAs in radiation environments. The FCC-phased CrFeCoNi RSS was chosen as the central HEA due to its frequent template material to develop other compositions. It was shown that CrFeCoNi has higher G_{e-ph} and C_e throughout the studied electronic temperate range (up to 3×10^4 K) compared to its constituent elements. Using $\ell/2T$ -MD, we demonstrated that CrFeCoNi was more effective in dissipating excess energy during cascade events via local plasmons, leading to lesser defect formation and higher defect recombination than the elemental Ni. Moreover, this work demonstrated the crucial roles of electronic and phonon effects during cascade events.

Analysis of individual affinity for defect formation of the PEs in CrFeCoNi showed that the elements such as Cr and partially Ni tend to

form more FPs due to their relatively lower v_f^1 energies than with the remaining elements. It motivated us to explore the non-equimolar RSS to improve the radiation-damage resistance further. A set of representative non-equimolar RSS compositions were investigated to understand electronic and phonon properties. Lower Cr or Ni concentration (keeping the remaining three PEs equimolar among themselves) lead to slightly lower G_{e-ph} and higher κ_e . Reduction of Fe or Co had negligible effects on G_{e-ph} . Moving away from the non-equimolar case led to relatively poorer performance in e – ph – assisted heat dissipation, while it improved energy exchange among electrons of neighboring atoms.

The addition of Al, Mn and Cu to CrFeCoNi was investigated as another strategy. We demonstrated that the equimolar addition of Al substantially increased G_{e-ph} , which is a critical factor for plasmon excitations and to reduce defect formation. While the equimolar addition of Mn slightly improved G_{e-ph} , the equimolar addition of Cu worsens it. On the other hand, adding any of these elements substantially improved κ_e . These general trends indicated that the addition of lighter elements compared to the averaged atomic mass improves G_{e-ph} , considering that atomic mass is used when normalizing phonon modes. On the other hand, the addition of atoms with more differing VEC led to higher κ_e due to higher v_F , despite shorter-living plasmons when adding lighter elements.

Electronic properties were then integrated into the $\ell/2T$ -MD model to investigate their effect in FPs formation. We found that the electronic properties play a critical role in determining the steady-state FPs number after the PKA event. Neglecting these effects lead to errors of about $\sim 20 - 25\%$ between classical MD and $\ell/2T$ -MD at 50 keV PKA energy. We also investigated the fraction of FPs per principal element in the HEA. We found that elements with smaller vacancy formation energies (i.e., Cr and Ni) resulted in more FPs, whereas elements with higher formation energy (i.e., Fe and Co) showed fewer FPs. This finding suggests the possibility of exploring non-equimolar HEA compositions to obtain optimal radiation resistance combining optimal electronic and lattice properties.

Declaration of Competing Interest

The authors declare that they have no known competing financial interests or personal relationships that could have appeared to influence the work reported in this paper.

Acknowledgment

We acknowledge the support of New Frontiers in Research Fund (NFRFE-2019-01095) and from the Natural Sciences and Engineering Research Council of Canada (NSERC) through the Discovery Grant under Award Application Number 2016-06114. M.H. gratefully acknowledges the financial support from the Department of Mechanical Engineering at UBC through the Four Years Fellowship. This research partially was supported through computational resources and services provided by Advanced Research Computing at the University of British Columbia.

Supplementary material

Supplementary material associated with this article can be found, in the online version, at doi:[10.1016/j.actamat.2022.118511](https://doi.org/10.1016/j.actamat.2022.118511).

References

- [1] B. Cantor, I. Chang, P. Knight, A. Vincent, Microstructural development in equiatomic multicomponent alloys, Materials Science and Engineering: A 375–377 (2004) 213–218, <https://doi.org/10.1016/j.msea.2003.10.257> <http://www.sciencedirect.com/science/article/pii/S0921509303009936>
- [2] J.-W. Yeh, S.-K. Chen, S.-J. Lin, J.-Y. Gan, T.-S. Chin, T.-T. Shun, C.-H. Tsau, S.-Y. Chang, Nanostructured high-entropy alloys with multiple principal elements:

- novel alloy design concepts and outcomes, *Adv Eng Mater* 6 (5) (2004) 299–303, <https://doi.org/10.1002/adem.200300567>.
- [3] J.W. Yeh, Recent progress in high-entropy alloys, *Annales de Chimie. Science des Materiaux* 31 (6) (2006) 633–648, http://www.inis.iaea.org/search/search.aspx?orig_q=RN:38042167
- [4] O.N. Senkov, J.M. Scott, S.V. Senkova, F. Meisenkothen, D.B. Miracle, C. F. Woodward, Microstructure and elevated temperature properties of a refractory tanbhfrzti alloy, *J Mater Sci* 47 (9) (2012) 4062–4074, <https://doi.org/10.1007/s10853-012-6260-2>.
- [5] K.-H. Cheng, C.-H. Lai, S.-J. Lin, J.-W. Yeh, Structural and mechanical properties of multi-element (alcrmatitiz)nx coatings by reactive magnetron sputtering, *Thin Solid Films* 519 (10) (2011) 3185–3190, <https://doi.org/10.1016/j.tsf.2010.11.034>, <http://www.sciencedirect.com/science/article/pii/S0040609010015701>
- [6] A. Gali, E. George, Tensile properties of high- and medium-entropy alloys, *Intermetallics* 39 (2013) 74–78, <https://doi.org/10.1016/j.intermet.2013.03.018>, <http://www.sciencedirect.com/science/article/pii/S096979513000903>
- [7] J. Chen, P. Niu, Y. Liu, Y. Lu, X. Wang, Y. Peng, J. Liu, Effect of zr content on microstructure and mechanical properties of alcocrfeni high entropy alloy, *Materials & Design* 94 (2016) 39–44, <https://doi.org/10.1016/j.matdes.2016.01.033>, <http://www.sciencedirect.com/science/article/pii/S026412751630034X>
- [8] X. Xian, Z. Zhong, B. Zhang, K. Song, C. Chen, S. Wang, J. Cheng, Y. Wu, A high-entropy v35ti35fe15cr10zr5 alloy with excellent high-temperature strength, *Materials & Design* 121 (2017) 229–236, <https://doi.org/10.1016/j.matdes.2017.02.029>, <http://www.sciencedirect.com/science/article/pii/S0264127517301570>
- [9] J. Li, Q. Fang, B. Liu, Y. Liu, Transformation induced softening and plasticity in high entropy alloys, *Acta Mater* 147 (2018) 35–41, <https://doi.org/10.1016/j.actamat.2018.01.002>, <http://www.sciencedirect.com/science/article/pii/S13596418300338>
- [10] Y. Cai, G. Wang, Y. Ma, Z. Cao, X. Meng, High hardness dual-phase high entropy alloy thin films produced by interface alloying, *Scr Mater* 162 (2019) 281–285, <https://doi.org/10.1016/j.scriptamat.2018.11.004>, <http://www.sciencedirect.com/science/article/pii/S1359646218306857>
- [11] P.-K. Huang, J.-W. Yeh, T.-T. Shun, S.-K. Chen, Multi-principal-element alloys with improved oxidation and wear resistance for thermal spray coating, *Adv Eng Mater* 6 (1) (2004) 74–78, <https://www.scopus.com/inward/record.uri?eid=2-s2.0-1642324318&partnerID=40&md5=3cd7f0900c67f4654c958e7c949372ae>
- [12] C.-Y. Hsu, J.-W. Yeh, S.-K. Chen, T.-T. Shun, Wear resistance and high-temperature compression strength of fcc cuconical0.5fe alloy with boron addition, *Metallurgical and Materials Transactions A* 35 (5) (2004) 1465–1469, <https://doi.org/10.1007/s11661-004-0254-x>
- [13] N. Kumar, M. Fusco, M. Komarasamy, R. Mishra, M. Bourham, K. Murty, Understanding effect of 3.5 wt. corrosion of al0.1cofceni high-entropy alloy, *J. Nucl. Mater.* 495 (2017) 154–163, <https://doi.org/10.1016/j.jnucmat.2017.08.015>, <http://www.sciencedirect.com/science/article/pii/S0022311517307754>
- [14] Z. Wu, H. Bei, G. Pharr, E. George, Temperature dependence of the mechanical properties of equiatomic solid solution alloys with face-centered cubic crystal structures, *Acta Mater* 81 (2014) 428–441, <https://doi.org/10.1016/j.actamat.2014.08.026>, <http://www.sciencedirect.com/science/article/pii/S1359641006272>
- [15] B. Gludovatz, A. Hohenwarter, D. Catooor, E.H. Chang, E.P. George, R.O. Ritchie, A fracture-resistant high-entropy alloy for cryogenic applications, *Science* 345 (6201) (2014) 1153–1158, <https://doi.org/10.1126/science.1254581>, <https://science.sciencemag.org/content/345/6201/1153>
- [16] Z. Wu, H. Bei, F. Otto, G. Pharr, E. George, Recovery, recrystallization, grain growth and phase stability of a family of fcc-structured multi-component equiatomic solid solution alloys, *Intermetallics* 46 (2014) 131–140, <https://doi.org/10.1016/j.intermet.2013.10.024>, <http://www.sciencedirect.com/science/article/pii/S0966979513002872>
- [17] M.-H. Chuang, M.-H. Tsai, W.-R. Wang, S.-J. Lin, J.-W. Yeh, Microstructure and wear behavior of alxco1.5crfeni1.5tiy high-entropy alloys, *Acta Mater* 59 (16) (2011) 6308–6317, <https://doi.org/10.1016/j.actamat.2011.06.041>, <http://www.sciencedirect.com/science/article/pii/S1359645411004551>
- [18] M.W. Ullah, D.S. Aidhy, Y. Zhang, W.J. Weber, Damage accumulation in ion-irradiated ni-based concentrated solid-solution alloys, *Acta Mater* 109 (2016) 17–22, <https://doi.org/10.1016/j.actamat.2016.02.048>, <http://www.sciencedirect.com/science/article/pii/S1359645416301227>
- [19] C.-J. Tong, Y.-L. Chen, J.-W. Yeh, S.-J. Lin, S.-K. Chen, T.-T. Shun, C.-H. Tsau, S.-Y. Chang, Microstructure characterization of alxcrcufeni high-entropy alloy system with multiprincipal elements, *Metallurgical and Materials Transactions A* 36 (4) (2005) 881–893, <https://doi.org/10.1007/s11661-005-0283-0>.
- [20] D.F. Rojas, H. Li, O.K. Orhan, C. Shao, J.D. Hogan, M. Ponga, Mechanical and microstructural properties of a cocrfe0.75nimo0.3nb0.125 high-entropy alloy additively manufactured via cold-spray, *J Alloys Compd* 893 (2022) 162309, <https://doi.org/10.1016/j.jallcom.2021.162309>, <http://www.sciencedirect.com/science/article/pii/S0925838821037191>
- [21] O.K. Orhan, M. Islet, L. Caparini, M. Ponga, Exploring the compositional space of high-entropy alloys for cost-effective high-temperature applications, *Front. Mater* 8 (2022), <https://doi.org/10.3389/fmats.2021.816610>, <http://www.frontiersin.org/article/10.3389/fmats.2021.816610>
- [22] G. Was, R. Averback, 1.07 - Radiation Damage Using Ion Beams, in: R.J. Konings (Ed.), *Comprehensive Nuclear Materials*, Elsevier, Oxford, 2012, pp. 195–221, <https://doi.org/10.1016/B978-0-08-056033-5.00007-0>, <https://www.sciencedirect.com/science/article/pii/B9780080560335000070>
- [23] K.-Y. Tsai, M.-H. Tsai, J.-W. Yeh, Sluggish diffusion in co-cr-fe-mn-ni high-entropy alloys, *Acta Mater* 61 (13) (2013) 4887–4897, <https://doi.org/10.1016/j.actamat.2013.04.058>, <http://www.sciencedirect.com/science/article/pii/S1359645413003431>
- [24] X. Zhang, Gold nanoparticles: recent advances in the biomedical applications, *Cell Biochem. Biophys* 72 (3) (2015) 771–775, <https://doi.org/10.1007/s12013-015-0529-4>
- [25] T. Nagase, P.D. Rack, J.H. Noh, T. Egami, In-situ tem observation of structural changes in nano-crystalline cocrucufeni multicomponent high-entropy alloy (hea) under fast electron irradiation by high voltage electron microscopy (hvem), *Intermetallics* 59 (2015) 32–42, <https://doi.org/10.1016/j.intermet.2014.12.007>, <http://www.sciencedirect.com/science/article/pii/S096979514003112>
- [26] M. Dada, P. Popoola, S. Adeosun, N.R. Mathe, *High Entropy Alloys for Aerospace Applications*, IntechOpen, 2019.
- [27] S.-q. Xia, Z. Wang, T.-f. Yang, Y. Zhang, Irradiation behavior in high entropy alloys, *J. Iron. Steel. Res. Int* 22 (10) (2015) 879–884, [https://doi.org/10.1016/S1006-706X\(15\)30084-4](https://doi.org/10.1016/S1006-706X(15)30084-4).
- [28] O. Deluigi, R. Pasianot, F. Valencia, A. Caro, D. Farkas, E. Bringa, Simulations of primary damage in a high entropy alloy: probing enhanced radiation resistance, *Acta Mater* 213 (2021) 116951, <https://doi.org/10.1016/j.actamat.2021.116951>, <http://www.sciencedirect.com/science/article/pii/S1359645421003311>
- [29] G. Battistoni, T. Boehlen, F. Cerutti, P.W. Chin, L.S. Esposito, A. Fassò, A. Ferrari, A. Lechner, A. Empl, A. Mairani, A. Mereghetti, P.G. Ortega, J. Ranft, S. Roesler, P.R. Sala, V. VLachoudis, G. Smirnov, Overview of the fluka code, *Annu Nucl Energy* 82 (2015) 10–18, <https://doi.org/10.1016/j.anucene.2014.11.007>, Joint International Conference on Supercomputing in Nuclear Applications and Monte Carlo 2013, SNA + MC 2013. Pluri- and Trans-disciplinarity, Towards New Modeling and Numerical Simulation Paradigms
- [30] P.G. Klemens, R.K. Williams, Thermal conductivity of metals and alloys, *International Metals Reviews* 31 (1) (1986) 197–215, <https://doi.org/10.1179/imr.1986.31.1.197>.
- [31] J.M. Ziman, *Principles of the theory of solids*, 2, Cambridge University Press, 1972, <https://doi.org/10.1017/CBO9781139644075>.
- [32] R.E.B. Makinson, *The thermal conductivity of metals*. Mathematical Proceedings of the Cambridge Philosophical Society volume 34 (3), Cambridge University Press, 1938, pp. 474–497.
- [33] N.K. Kumar, C. Li, K. Leonard, H. Bei, S. Zinkle, Microstructural stability and mechanical behavior of fenimcnr high entropy alloy under ion irradiation, *Acta Mater* 113 (2016) 230–244, <https://doi.org/10.1016/j.actamat.2016.05.007>, <http://www.sciencedirect.com/science/article/pii/S1359645416303342>
- [34] F. Granberg, K. Nordlund, M.W. Ullah, K. Jin, C. Lu, H. Bei, L.M. Wang, F. Djurabekova, W.J. Weber, Y. Zhang, Mechanism of radiation damage reduction in equiatomic multicomponent single phase alloys, *Phys. Rev. Lett.* 116 (2016) 135504, <https://doi.org/10.1103/PhysRevLett.116.135504>, <http://link.aps.org/doi/10.1103/PhysRevLett.116.135504>
- [35] C. Lu, L. Niu, N. Chen, K. Jin, T. Yang, P. Xiu, Y. Zhang, F. Gao, H. Bei, S. Shi, M.-R. He, I.M. Robertson, W.J. Weber, L. Wang, Enhancing radiation tolerance by controlling defect mobility and migration pathways in multicomponent single-phase alloys, *Nat Commun* 7 (1) (2016) 13564, <https://doi.org/10.1038/ncomms13564>.
- [36] C.M. Barr, J.E. Nathaniel, K.A. Unocic, J. Liu, Y. Zhang, Y. Wang, M.L. Taheri, Exploring radiation induced segregation mechanisms at grain boundaries in equiatomic cocrfennm high entropy alloy under heavy ion irradiation, *Scr Mater* 156 (2018) 80–84, <https://doi.org/10.1016/j.scriptamat.2018.06.041>, <http://www.sciencedirect.com/science/article/pii/S1359646218304068>
- [37] Z. Lin, L.V. Zhigilei, Temperature dependences of the electron-phonon coupling, electron heat capacity and thermal conductivity in ni under femtosecond laser irradiation, *Appl Surf Sci* 253 (15) (2007) 6295–6300, <https://doi.org/10.1016/j.apsusc.2007.01.032>, Proceedings of the Fifth International Conference on Photo-Excited Processes and Applications
- [38] D. Duffy, A. Rutherford, Including the effects of electronic stopping and electron-ion interactions in radiation damage simulations, *J. Phys.: Condens. Matter* 19 (2011) 016207.
- [39] A. Tamm, G. Samolyuk, A.A. Correa, M. Klintenberg, A. Aabloo, A. Caro, Electron-phonon interaction within classical molecular dynamics, *Phys. Rev. B* 94 (2016) 024305, <https://doi.org/10.1103/PhysRevB.94.024305>, <http://link.aps.org/doi/10.1103/PhysRevB.94.024305>
- [40] A. Tamm, M. Caro, A. Caro, G. Samolyuk, M. Klintenberg, A.A. Correa, Langevin dynamics with spatial correlations as a model for electron-phonon coupling, *Phys. Rev. Lett.* 120 (2018) 185501, <https://doi.org/10.1103/PhysRevLett.120.185501>.
- [41] A. Tamm, M. Caro, A. Caro, A.A. Correa, Role of electrons in collision cascades in solids. ii. molecular dynamics, *Phys. Rev. B* 99 (2019) 174302, <https://doi.org/10.1103/PhysRevB.99.174302>.
- [42] E. Zarkadoula, G. Samolyuk, W.J. Weber, Effects of electron-phonon coupling on damage accumulation in molecular dynamics simulations of irradiated nickel, *Materials Research Letters* 7 (12) (2019) 490–495, <https://doi.org/10.1080/21663831.2019.1659435>.
- [43] E. Zarkadoula, G. Samolyuk, W.J. Weber, Effects of electron-phonon coupling on damage accumulation in molecular dynamics simulations of irradiated nickel, *Materials Research Letters* 7 (12) (2019) 490–495, <https://doi.org/10.1080/21663831.2019.1659435>.

- [44] E. Zarkadoula, D.M. Duffy, K. Nordlund, M.A. Seaton, I.T. Todorov, W.J. Weber, K. Trachenko, Electronic effects in high-energy radiation damage in tungsten, *J. Phys.: Condens. Matter* 27 (13) (2015) 135401, <https://doi.org/10.1088/0953-8984/27/13/135401>.
- [45] E. Zarkadoula, G. Samolyuk, W.J. Weber, Two-temperature model in molecular dynamics simulations of cascades in ni-based alloys, *J Alloys Compd* 700 (2017) 106–112, <https://doi.org/10.1016/j.jallcom.2016.12.441>.<https://www.sciencedirect.com/science/article/pii/S0925838816343705>
- [46] M.W. Ullah, M. Ponga, A new approach for electronic heat conduction in molecular dynamics simulations, *Modell. Simul. Mater. Sci. Eng* 27 (7) (2019) 075008, <https://doi.org/10.1088/1361-651x/ab309f>.
- [47] M.W. Ullah, N. Sellami, A. Leino, H. Bei, Y. Zhang, W.J. Weber, Electron-phonon coupling induced defect recovery and strain relaxation in ni and equiatomic nife alloy, *Comput. Mater. Sci.* 173 (2020) 109394, <https://doi.org/10.1016/j.commatsci.2019.109394>.<https://www.sciencedirect.com/science/article/pii/S0927025619306937>
- [48] J. Grossi, J. Kohanoff, E.M. Bringa, MeV Irradiation of tungsten nanowires: structural modifications, *Mater. Res. Express* 7 (5) (2020) 055015, <https://doi.org/10.1088/2053-1591/ab9254>.
- [49] M. Ponga, K. Bhattacharya, M. Ortiz, A sublinear-scaling approach to density-functional-theory analysis of crystal defects, *J Mech Phys Solids* 95 (2016) 530–556, <https://doi.org/10.1016/j.jmps.2016.05.029>.<https://www.sciencedirect.com/science/article/pii/S0022509616303489>
- [50] M. Ponga, K. Bhattacharya, M. Ortiz, Large scale *ab-initio* simulations of dislocations, *J Comput Phys* 407 (2020) 109249, <https://doi.org/10.1016/j.jcp.2020.109249>.<https://www.sciencedirect.com/science/article/pii/S00219999120300231>
- [51] A. Zunger, S.-H. Wei, L.G. Ferreira, J.E. Bernard, Special quasirandom structures, *Phys. Rev. Lett.* 65 (1990) 353–356, <https://doi.org/10.1103/PhysRevLett.65.353>.
- [52] S.-H. Wei, L.G. Ferreira, J.E. Bernard, A. Zunger, Electronic properties of random alloys: special quasirandom structures, *Phys. Rev. B* 42 (1990) 9622–9649, <https://doi.org/10.1103/PhysRevB.42.9622>.
- [53] M.C. Gao, C. Niu, C. Jiang, D.L. Irving, *Applications of Special Quasi-random Structures to High-Entropy Alloys*, Springer International Publishing, Cham, 2016, pp. 333–368.
- [54] P. Soven, Coherent-potential model of substitutional disordered alloys, *Phys. Rev.* 156 (1967) 809–813, <https://doi.org/10.1103/PhysRev.156.809>.
- [55] D.W. Taylor, Vibrational properties of imperfect crystals with large defect concentrations, *Phys. Rev.* 156 (1967) 1017–1029, <https://doi.org/10.1103/PhysRev.156.1017>.
- [56] J. Korringa, On the calculation of the energy of a bloch wave in a metal, *Physica* 13 (6) (1947) 392–400, [https://doi.org/10.1016/0031-8914\(47\)90013-X](https://doi.org/10.1016/0031-8914(47)90013-X).<https://www.sciencedirect.com/science/article/pii/003189144790013X>
- [57] W. Kohn, N. Rostoker, Solution of the schrödinger equation in periodic lattices with an application to metallic lithium, *Phys. Rev.* 94 (1954) 1111–1120, <https://doi.org/10.1103/PhysRev.94.1111>.
- [58] L. Vitos, Total-energy method based on the exact muffin-tin orbitals theory, *Phys. Rev. B* 64 (2001) 014107, <https://doi.org/10.1103/PhysRevB.64.014107>.
- [59] F. Tian, Y. Wang, D.L. Irving, L. Vitos, *Applications of Coherent Potential Approximation to HEAs*, Springer International Publishing, Cham, 2016, pp. 299–332.
- [60] T. Fukushima, H. Akai, T. Chikyow, H. Kino, Automatic exhaustive calculations of large material space by korringa-kohn-rostoker coherent potential approximation method applied to equiatomic quaternary high entropy alloys, *Phys. Rev. Materials* 6 (2022) 023802, <https://doi.org/10.1103/PhysRevMaterials.6.023802>.
- [61] J. Zhai, R. Xue, Z. Cheng, Y. Ke, Direct comparison of auxiliary and itinerant coherent potential approximations for disordered lattice vibration: phonon spectral and transport properties, *Phys. Rev. B* 104 (2021) 024205, <https://doi.org/10.1103/PhysRevB.104.024205>.
- [62] G.D. Samolyuk, L.K. Béland, G.M. Stocks, R.E. Stoller, Electron-phonon coupling in ni-based binary alloys with application to displacement cascade modeling, *J. Phys.: Condens. Matter* 28 (17) (2016) 175501, <https://doi.org/10.1088/0953-8984/28/17/175501>.
- [63] L. Bellaiche, D. Vanderbilt, Virtual crystal approximation revisited: application to dielectric and piezoelectric properties of perovskites, *Phys. Rev. B* 61 (2000) 7877–7882, <https://doi.org/10.1103/PhysRevB.61.7877>.
- [64] V. Heine, The Pseudopotential Concept, in: *Solid State Physics*, volume 24, Academic Press, 1970, pp. 1–36, [https://doi.org/10.1016/S0081-1947\(08\)60069-7](https://doi.org/10.1016/S0081-1947(08)60069-7).<https://www.sciencedirect.com/science/article/pii/S0081194708600697>
- [65] F. Tian, A review of solid-solution models of high-entropy alloys based on ab initio calculations, *Front. Mater* 4 (2017) 36, <https://doi.org/10.3389/fmats.2017.00036>.<https://www.frontiersin.org/article/10.3389/fmats.2017.00036>
- [66] A. Caro, A.A. Correa, A. Tamm, G.D. Samolyuk, G.M. Stocks, Adequacy of damped dynamics to represent the electron-phonon interaction in solids, *Phys. Rev. B* 92 (2015) 144309, <https://doi.org/10.1103/PhysRevB.92.144309>.
- [67] E. Zarkadoula, G. Samolyuk, H. Xue, H. Bei, W.J. Weber, Effects of two-temperature model on cascade evolution in ni and nife, *Scr Mater* 124 (2016) 6–10, <https://doi.org/10.1016/j.scriptamat.2016.06.028>.<https://www.sciencedirect.com/science/article/pii/S1359646216302822>
- [68] E. Zarkadoula, G. Samolyuk, W.J. Weber, Effects of electronic excitation on cascade dynamics in nickel-iron and nickel-palladium systems, *Scr Mater* 138 (2017) 124–129, <https://doi.org/10.1016/j.scriptamat.2017.05.041>.<https://www.sciencedirect.com/science/article/pii/S1359646217302932>
- [69] M. Ponga, D. Sun, A unified framework for heat and mass transport at the atomic scale, *Modell. Simul. Mater. Sci. Eng* 26 (3) (2018) 035014, <https://doi.org/10.1088/1361-651x/aaaf94>.
- [70] O.K. Orhan, M. Hendy, M. Ponga, Temperature-dependent first-principles electronic, and phonon properties, and molecular dynamics of defect evolution, 2022, (<https://github.com/Mponga/Radiation-Damage-in-High-Entropy-Alloys>).
- [71] P.B. Allen, Theory of thermal relaxation of electrons in metals, *Phys. Rev. Lett.* 59 (1987) 1460–1463, <https://doi.org/10.1103/PhysRevLett.59.1460>.
- [72] Z. Li, C. Wang, W. Wang, C. Li, P. Zhang, Temperature and compression effects on electron heat capacity and electron-phonon coupling in aluminum and beryllium: insights from ab initio simulations, *Phys Plasmas* 22 (11) (2015) 112705, <https://doi.org/10.1063/1.4935843>.
- [73] P. Hohenberg, W. Kohn, Inhomogeneous electron gas, *Phys. Rev.* 136 (1964) B864–B871, <https://doi.org/10.1103/PhysRev.136.B864>.
- [74] W. Kohn, L.J. Sham, Self-consistent equations including exchange and correlation effects, *Phys. Rev.* 140 (1965) A1133–A1138, <https://doi.org/10.1103/PhysRev.140.A1133>.
- [75] D.C. Langreth, J.P. Perdew, Theory of nonuniform electronic systems. i. analysis of the gradient approximation and a generalization that works, *Phys. Rev. B* 21 (1980) 5469–5493, <https://doi.org/10.1103/PhysRevB.21.5469>.
- [76] J.P. Perdew, Density-functional approximation for the correlation energy of the inhomogeneous electron gas, *Phys. Rev. B* 33 (1986) 8822–8824, <https://doi.org/10.1103/PhysRevB.33.8822>.
- [77] J.P. Perdew, J.A. Chevary, S.H. Vosko, K.A. Jackson, M.R. Pederson, D.J. Singh, C. Fiolhais, Atoms, molecules, solids, and surfaces: applications of the generalized gradient approximation for exchange and correlation, *Phys. Rev. B* 46 (1992) 6671–6687, <https://doi.org/10.1103/PhysRevB.46.6671>.
- [78] X. Gonze, First-principles responses of solids to atomic displacements and homogeneous electric fields: implementation of a conjugate-gradient algorithm, *Phys. Rev. B* 55 (1997) 10337–10354, <https://doi.org/10.1103/PhysRevB.55.10337>.
- [79] X. Gonze, C. Lee, Dynamical matrices, born effective charges, dielectric permittivity tensors, and interatomic force constants from density-functional perturbation theory, *Phys. Rev. B* 55 (1997) 10355–10368, <https://doi.org/10.1103/PhysRevB.55.10355>.
- [80] L. Nordheim, Zur elektronentheorie der metalle. i, *Ann Phys* 401 (5) (1900) 607–640, <https://doi.org/10.1002/andp.19314010507>.
- [81] A. Pribram-Jones, S. Pittalis, E.K.U. Gross, K. Burke, Thermal density functional theory in context, in: F. Graziani, M.P. Desjarlais, R. Redmer, S.B. Trickey (Eds.), *Frontiers and Challenges in Warm Dense Matter*, Springer International Publishing, Cham, 2014, pp. 25–60.
- [82] P. Hofmann, I.Y. Sklyadneva, E.D.L. Rienks, E.V. Chulkov, Electron-phonon coupling at surfaces and interfaces, *New J Phys* 11 (12) (2009) 125005, <https://doi.org/10.1088/1367-2630/11/12/125005>.
- [83] S. Ponc, E. Margine, C. Verdi, F. Giustino, Epw: electron-phonon coupling, transport and superconducting properties using maximally localized wannier functions, *Comput Phys Commun* 209 (2016) 116–133, <https://doi.org/10.1016/j.cpc.2016.07.028>.<http://www.sciencedirect.com/science/article/pii/S0010465516302260>
- [84] M.H. Cohen, Optical constants, heat capacity and the fermi surface, *Philos. Mag* 3 (31) (1958) 762–775, <https://doi.org/10.1080/1478643580237011>.
- [85] O.K. Orhan, D.D. O'Regan, Plasmonic performance of $\text{au}_{x}\text{ag}_{y}\text{cu}_{1-x-y}$ alloys from many-body perturbation theory, *J. Phys.: Condens. Matter* 31 (31) (2019) 315901, <https://doi.org/10.1088/1361-648x/ab1c30>.
- [86] O.K. Orhan, Quantum espresso post-processing tool to calculate the drude plasmon energy, 2020, (<https://github.com/okorhan/Drude-plasmon-energy>).
- [87] O.K. Orhan, M. Ponga, Surface-plasmon properties of noble metals with exotic phases, *The Journal of Physical Chemistry C* 125 (39) (2021) 21521–21532, <https://doi.org/10.1021/acs.jpcc.1c06110>.
- [88] G. Grimvall, The electron-phonon interaction in normal metals, *Phys. Scr* 14 (1–2) (1976) 63–78, <https://doi.org/10.1088/0031-8949/14/1-2/013>.
- [89] V. Gasparov, R. Huguenin, Electron-phonon, electron-electron and electron-surface scattering in metals from ballistic effects, *Adv Phys* 44 (4) (1993) 393–521, <https://doi.org/10.1080/00018739300101514>.
- [90] S. Ogawa, H. Nagano, H. Petek, Hot-electron dynamics at cu(100), cu(110), and cu(111) surfaces: comparison of experiment with fermi-liquid theory, *Phys. Rev. B* 55 (1997) 10869–10877, <https://doi.org/10.1103/PhysRevB.55.10869>.
- [91] S. Dal Forno, L. Ranno, J. Lischner, Material, size, and environment dependence of plasmon-induced hot carriers in metallic nanoparticles, *The Journal of Physical Chemistry C* 122 (15) (2018) 8517–8527, <https://doi.org/10.1021/acs.jpcc.8b00651>.
- [92] I.Y. Sklyadneva, E.V. Chulkov, W.-D. Schöne, V.M. Silkin, R. Keyling, P. M. Echenique, Role of electron-phonon interactions versus electron-electron interactions in the broadening mechanism of the electron and hole linewidths in bulk bc, *Phys. Rev. B* 71 (2005) 174302, <https://doi.org/10.1103/PhysRevB.71.174302>.
- [93] P. Giannozzi, S. Baroni, N. Bonini, M. Calandra, R. Car, C. Cavazzoni, D. Ceresoli, G.L. Chiarotti, M. Cococcioni, I. Dabo, A.D. Corso, S. de Gironcoli, S. Fabris, G. Fratesi, R. Gebauer, U. Gerstmann, C. GouLoussis, A. Kokalj, M. Lazzeri, L. Martin-Samios, N. Marzari, F. Mauri, R. Mazzarello, S. Paolini, A. Pasquarello, L. Paulatto, C. Sbraccia, S. Scandolo, G. Scalauzero, A.P. Seitsonen, A. Smogunov, P. Umari, R.M. Wentzcovitch, Quantum espresso: a modular and open-source

- software project for quantum simulations of materials, *J. Phys.: Condens. Matter* 21 (39) (2009) 395502.<http://stacks.iop.org/0953-8984/21/i=39/a=395502>
- [94] P. Giannozzi, O. Andreussi, T. Brumme, O. Bunau, M.B. Nardelli, M. Calandra, R. Car, C. Cavazzoni, D. Ceresoli, M. Cococcioni, N. Colonna, I. Carmimeo, A. D. Corso, S. de Gironcoli, P. Delugas, R.A.D. Jr, A. Ferretti, A. Floris, G. Fratesi, G. Fugallo, R. Gebauer, U. Gerstmann, F. Giustino, T. Gorni, J. Jia, M. Kawamura, H.-Y. Ko, A. Kokalj, E. Küçükbenli, M. Lazzeri, M. Marsili, N. Marzari, F. Mauri, N. L. Nguyen, H.-V. Nguyen, A.O. de-la Roza, L. Paulatto, S. Ponc, D. Rocca, R. Sabatini, B. Santra, M. Schlipf, A.P. Seitsonen, A. Smogunov, I. Timrov, T. Thonhauser, P. Umari, N. Vast, X. Wu, S. Baroni, Advanced capabilities for materials modelling with q uantum espresso, *J. Phys.: Condens. Matter* 29 (46) (2017) 465901.<http://stacks.iop.org/0953-8984/29/i=46/a=465901>
- [95] Thermo_pw:Ab-initio computation of material properties, (https://www.dalcorso.github.io/thermo_pw/). Accessed: 18.09.
- [96] D.R. Hamann, Optimized norm-conserving vanderbilt pseudopotentials, *Phys. Rev. B* 88 (2013) 085117, <https://doi.org/10.1103/PhysRevB.88.085117>.
- [97] M. Schlipf, F. Gygi, Optimization algorithm for the generation of oncv pseudopotentials, *Comput Phys Commun* 196 (2015) 36–44, <https://doi.org/10.1016/j.cpc.2015.05.011>.<http://www.sciencedirect.com/science/article/pii/S0010465515001897>
- [98] D.R. Hamann, M. Schlüter, C. Chiang, Norm-conserving pseudopotentials, *Phys. Rev. Lett.* 43 (1979) 1494–1497, <https://doi.org/10.1103/PhysRevLett.43.1494>.
- [99] G.P. Kerker, Non-singular atomic pseudopotentials for solid state applications, *J. Phys. C: Solid State Phys* 13 (9) (1980) L189–L194, <https://doi.org/10.1088/0022-3719/13/9/004>.
- [100] D.R. Hamann, Generalized norm-conserving pseudopotentials, *Phys. Rev. B* 40 (1989) 2980–2987, <https://doi.org/10.1103/PhysRevB.40.2980>.
- [101] M. Palumbo, A.D. Corso, Lattice dynamics and thermophysical properties of h.c.p. os and ru from the quasi-harmonic approximation, *J. Phys.: Condens. Matter* 29 (39) (2017) 395401, <https://doi.org/10.1088/1361-648x/aa7dca>.
- [102] F. Tian, L.K. Varga, N. Chen, L. Delczeg, L. Vitos, Ab initio investigation of high-entropy alloys of 3d elements, *Phys. Rev. B* 87 (2013) 075144, <https://doi.org/10.1103/PhysRevB.87.075144>.
- [103] O.c.v. Schneeweiss, M. Friák, M. Dudová, D. Holec, M. Šob, D. Kriegner, V. Holý, P.c.v. Beran, E.P. George, J. Neugebauer, A. Dlouhý, Magnetic properties of the crmnfeconi high-entropy alloy, *Phys. Rev. B* 96 (2017) 014437, <https://doi.org/10.1103/PhysRevB.96.014437>.
- [104] J. Šebesta, K. Carva, D. Legut, Role of magnetism in the stability of the high-entropy alloy cocrfemnni and its derivatives, *Phys. Rev. Materials* 3 (2019) 124410, <https://doi.org/10.1103/PhysRevMaterials.3.124410>.
- [105] J. Zemann, Crystal structures, 2nd edition. vol. 1 by r. w. g. wyckoff, *Acta Crystallogr* 18 (1) (1965), <https://doi.org/10.1107/S0365110X65000361>.139–139
- [106] H.J. Monkhorst, J.D. Pack, Special points for brillouin-zone integrations, *Phys. Rev. B* 13 (1976) 5188–5192, <https://doi.org/10.1103/PhysRevB.13.5188>.
- [107] J.P. Mendez, M. Ponga, Mxe: a package for simulating long-term diffusive mass transport phenomena in nanoscale systems, *Comput Phys Commun* 260 (2021) 107315, <https://doi.org/10.1016/j.cpc.2020.107315>.<http://www.sciencedirect.com/science/article/pii/S0010465520301211>
- [108] S. Plimpton, Fast parallel algorithms for short-range molecular dynamics, *J Comput Phys* 117 (1) (1995) 1–19, <https://doi.org/10.1006/jcph.1995.1039>, <https://www.sciencedirect.com/science/article/pii/S002199918571039X>
- [109] D. Farkas, A. Caro, Model interatomic potentials and lattice strain in a high-entropy alloy, *J Mater Res* 33 (19) (2018) 3218–3225, <https://doi.org/10.1557/jmr.2018.245>.
- [110] L. Qian, H. Bao, R. Li, Q. Peng, Atomistic insights of a chemical complexity effect on the irradiation resistance of high entropy alloys, *Materials Advances* (2021).
- [111] J.A. Stewart, G. Brookman, P. Price, M. Franco, W. Ji, K. Hattar, R. Dingreville, Characterizing single isolated radiation-damage events from molecular dynamics via virtual diffraction methods, *J Appl Phys* 123 (16) (2018) 165902.
- [112] C.-W. Lee, J.A. Stewart, R. Dingreville, S.M. Foiles, A. Schleife, Multiscale simulations of electron and ion dynamics in self-irradiated silicon, *Phys. Rev. B* 102 (2020) 024107, <https://doi.org/10.1103/PhysRevB.102.024107>.
- [113] J.F. Ziegler, M. Ziegler, J. Biersack, Srim - the stopping and range of ions in matter (2010), *Nucl. Instrum. Methods Phys. Res., Sect. B* 268 (11) (2010) 1818–1823, <https://doi.org/10.1016/j.nimb.2010.02.091>.19th International Conference on Ion Beam Analysis
- [114] J.P. Biersack, J.F. Ziegler, The stopping and range of ions in solids, in: H. Ryssel, H. Glawischng (Eds.), *Ion Implantation Techniques*, Springer Berlin Heidelberg, Berlin, Heidelberg, 1982, pp. 122–156.
- [115] M.J.D. Powell, Nonconvex minimization calculations and the conjugate gradient method, in: D.F. Griffiths (Ed.), *Numerical Analysis*, Springer Berlin Heidelberg, Berlin, Heidelberg, 1984, pp. 122–141.
- [116] H. Tsuzuki, P.S. Branicio, J.P. Rino, Structural characterization of deformed crystals by analysis of common atomic neighborhood, *Comput Phys Commun* 177 (6) (2007) 518–523, <https://doi.org/10.1016/j.cpc.2007.05.018>.<http://www.sciencedirect.com/science/article/pii/S0010465507002536>
- [117] A. Stukowski, Visualization and analysis of atomistic simulation data with OVITO—the open visualization tool, *Modell. Simul. Mater. Sci. Eng* 18 (1) (2009) 015012, <https://doi.org/10.1088/0956-0393/18/1/015012>.
- [118] A. Stukowski, V.V. Bulatov, A. Arsenlis, Automated identification and indexing of dislocations in crystal interfaces, *Modell. Simul. Mater. Sci. Eng* 20 (8) (2012) 085007, <https://doi.org/10.1088/0956-0393/20/8/085007>.
- [119] A. Fernández-Caballero, M. Fedorov, J.S. Wróbel, P.M. Mummary, D. Nguyen-Manh, Configurational entropy in multicomponent alloys: matrix formulation from ab initio based hamiltonian and application to the fcc cr-fe-mn-ni system, *Entropy* 21 (1) (2019), <https://doi.org/10.3390/e21010068>.<http://www.mdpi.com/1099-4300/21/1/68>
- [120] M. Born, K. Huang, *Dynamical theory of crystal lattices*, in: Oxford classic texts in the physical sciences, Clarendon Press, Oxford, 1954.<https://www.cds.cern.ch/record/224197>
- [121] F. Mouhat, F.m.c.-X. Coudert, Necessary and sufficient elastic stability conditions in various crystal systems, *Phys. Rev. B* 90 (2014) 224104, <https://doi.org/10.1103/PhysRevB.90.224104>.
- [122] S.P. Rudin, Generalization of soft phonon modes, *Phys. Rev. B* 97 (2018) 134114, <https://doi.org/10.1103/PhysRevB.97.134114>.
- [123] K. Nordlund, S.J. Zinkle, A.E. Sand, F. Granberg, R.S. Averback, R. Stoller, T. Suzudo, L. Malerba, F. Banhart, W.J. Weber, F. Willaime, S.L. Dudarev, D. Simeone, Improving atomic displacement and replacement calculations with physically realistic damage models, *Nat Commun* 9 (1) (2018) 1084, <https://doi.org/10.1038/s41467-018-03415-5>.